TÜBİTAK

Turkish Journal of Earth Sciences

http://journals.tubitak.gov.tr/earth/

Research Article

Turkish J Earth Sci
(2016) 25: 367-391

doi:10.3906/yer-1511-10

Mineralogy, geochemistry, and depositional environment of the Beduh Shale (Lower Triassic), Northern Thrust Zone, Iraq

Faraj H. TOBIA*, Sirwa S. SHANGOLA
Department of Geology, College of Science, Salahaddin University, Erbil, Iraq

Received: 21.11.2015 • **Accepted/Published Online:** 09.05.2016 • **Final Version:** 09.06.2016

Abstract: Integrated mineralogical and geochemical methods are utilized to investigate the provenance, paleoweathering, and depositional setting of shale from the Lower Triassic Beduh Formation in the Northern Thrust Zone, Iraq. The ~64-m-thick Beduh Formation consists of calcareous shale and marl intercalations with thin calcareous sandstone interbeds. X-ray diffraction analysis revealed that clay minerals comprise illite, kaolinite, and chlorite, with a minor mixed layer of illite/smectite and illite/chlorite. Calcite and quartz are the main nonclay species with subordinate amounts of feldspar and hematite. The mineralogical and geochemical parameters of the shale (e.g., high content of illite and moderate illite crystallinity index, Al_2O_3/TiO_2, Th/Co, Cr/Th, and LREE/HREE ratios) indicate that they were derived from felsic and intermediate components. This is supported by the enrichment of LREEs, negative Eu anomaly, and depletion of HREEs. The discriminant function-based major element diagrams indicated that the origin of sediments was probably from passive (the Arabian Shield and the Rutba Uplift) and active (volcanic activity) tectonic environments. The source of sediments for the Beduh Formation was likely the Rutba Uplift and/or the plutonic-metamorphic complexes of the Arabian Shield located to the southwest of the basin. Paleoweathering indices such as the chemical index of alteration and chemical index of weathering, as well as the A-CN-K (Al_2O_3-CaO+Na_2O-K_2O) diagram of the shale of the Beduh Formation suggest that the source terrain was moderately to intensely chemically weathered. The Cu/Zn, U/Th, Ni/Co, and V/Cr ratios and negative Eu anomaly indicate the deposition of sediments under an oxygen-rich environment.

Key words: Beduh Formation, clay mineralogy, provenance, tectonic setting, paleoweathering, paleoredox

1. Introduction

Geochemical data of fine-grained clastic sedimentary rocks, such as shales and siltstones, have been used to evaluate the nature of the parent rock and intensity of weathering, as well as to identify the tectonic setting of the source region (Bhatia, 1983; Taylor and McLennan, 1985; Bhatia and Crook, 1986; McLennan, 1989; Feng and Kerrich, 1990; McLennan and Taylor, 1991; Cullers, 1994; Hemming et al., 1995; Jahn and Condie, 1995; Girty et al., 1996; Etemad-Saeed et al., 2011; Verma and Armstrong-Altrin, 2013; Armstrong-Altrin et al., 2015a; Tawfik et al., 2015). Terrigenous sediments may reflect the characteristics of their source rocks on the assumption that some trace elements (e.g., REEs, Th, Zr, and Hf) are transformed from the site of weathering to the sedimentary basin and their abundances will not change during weathering, sedimentary transport, diagenesis, or metamorphic processes (Taylor and McLennan, 1985; McLennan, 1989; McLennan and Taylor, 1991). Therefore, these terrigenous sediments can be able to preserve the characteristics of their parent rocks.

The siliciclastic-dominated Beduh Formation (Lower Triassic) was first described near Beduhe village in the Northern Thrust Zone by Wetzel in 1950, as 60-m-thick reddish brown to reddish purple shale and marl with thin ribs of limestone and sandy streaks (Bellen et al., 1959). The formation crops out in the Northern Thrust Zone, near the Iraqi-Turkish border (Figure 1). It is also exposed in the Khabour Valley near Nazdur village, Sirwan Gorge, and is penetrated in Well Atshan-1 and Well Jabal Kand-1 in North Iraq and Diwan in South Iraq (Buday, 1980; Jassim et al., 2006). Based on fossil contents, the Beduh Formation yields an Upper Induan/Olenekian age. Meanwhile, the formation is considered as an excellent marker horizon used in field and subsurface surveys and regional correlations (Bellen et al., 1959).

The Triassic formations in the Northern Thrust Zone in Iraq receive less attention compared with other younger rocks. This is not only due to limited exposures and exploration wells penetrating them but also could be attributed to their inaccessibility and political aspects. So far, no studies have been carried out concerning the

* Correspondence: farajabba58@gmail.com

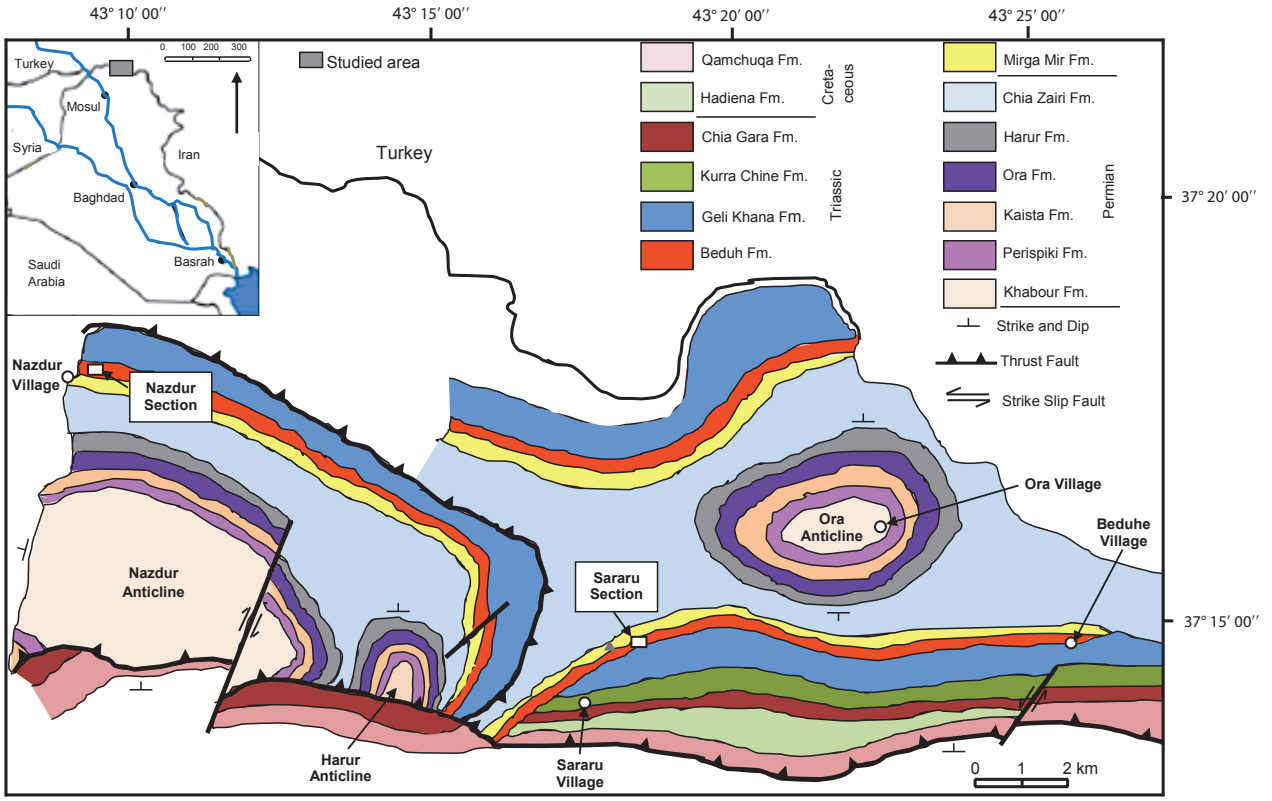

Figure 1. Geological map of the studied area showing the location of the sections (after Al-Brifkani, 2008).

mineralogy and geochemistry of the Beduh Formation. Most of the previous studies were related to structural, tectonic, and facies analyses. In 1997, Numan proposed the tectonic scenario of Iraq and suggested a slow rate of deposition for the Beduh Formation based on the plate tectonic stage at Triassic age, during separation of the Turkish Plate from the Arabian Plate. Later on, Al-Brifkani (2008) suggested that the studied area was divided by two major thrust faults, the Lower Southern Thrust and the Upper Northern Thrust. Recently, an oxidizing offshore-shoreface depositional setting was suggested for the Beduh Formation based on sedimentary structures and marine fossil contents (Hakeem, 2012).

The present study examines the mineralogy and geochemistry of the shales of the Beduh Formation that are exposed in the Northern Thrust Zone, northern Iraq (Figure 1). The objectives of this study are to investigate the source rock composition and paleoweathering intensity and to infer the tectonic setting of the basin during the Lower Triassic to deduce the depositional environment.

2. Geological setting

During the Late Permian epoch the Neo-Tethys Ocean started opening, then progressively widened during Early Triassic time (Figures 2 and 3). The Iranian Plate separated from the Arabian Plate in the Early Triassic, whereas the Turkish Plate separated from the Arabian Plate in Liassic time (Numan, 1997). A break-up unconformity formed along the northern and eastern margins of the Arabian Plate where Iraq forms its northeastern part. The Late Permian-Liassic megasequence was deposited on the N- and E-facing passive margin of the Arabian Plate. Thermal subsidence led to the formation of a passive margin megasequence along these margins and the development of the Mesopotamian Basin (Jassim et al., 2006).

The Rutba Basin, which had subsided in Earlier Paleozoic time, was gently inverted, forming the Rutba Uplift (contains thick Paleozoic sediments). The shoreline of the Late Permian basin was located along the eastern fault of the Rutba Uplift (Figure 2). The Rutba Subzone is the most extensive and uplifted part of the Rutba-Jezira, dominated by the huge Rutba Uplift active in Late Permian-Paleogene time. On the other hand, the Arabian Shield (AS) was composed of igneous-metamorphic complexes that were an elevated area at that time, located to the southwest of the basin of deposition. The Beduh Formation belongs to Tectonostratigraphic Megasequence AP6, which started from the Mid-Permian to Early Jurassic (255–182 Ma; Sharland et al., 2001).

The study area lies between 37°18′44″N and 37°15′02″N and 43°08′45″E and 43°18′19″E (Figure 1). In this area, the Beduh Formation is conformably succeeded by the Geli

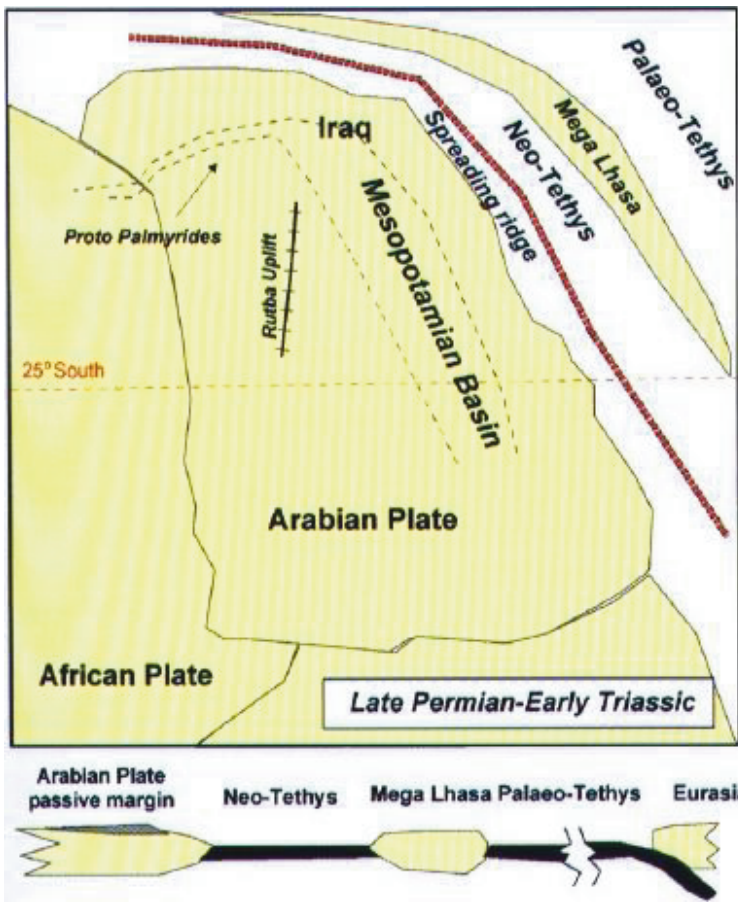

Figure 2. Late Permian-Early Triassic geodynamic development of the Arabian Plate (after Jassim and Goff, 2006).

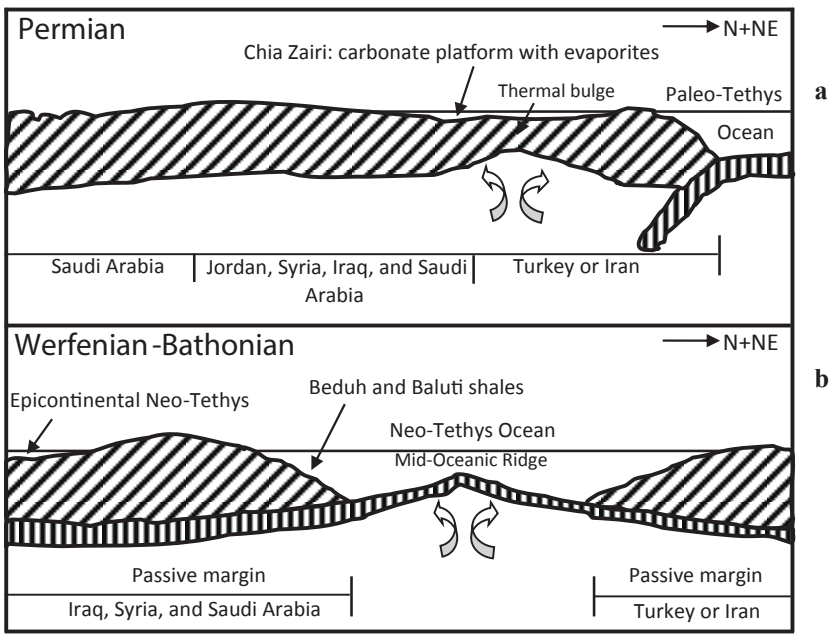

Figure 3. Imaginary model for the Permian-Triassic plate tectonic situation of Iraq and surrounding countries: a) intraplate set-up, b) rifting set-up (after Numan, 1997).

Khana Formation underlain by the Mirga Mir Formation (Bellen et al., 1959). The Beduh Formation attains a thickness of ~64 m and is composed of shale and marl and rare silt, with subordinate thin limestone interbeds and sandstone streaks (Figure 4). The succession is affected by two major thrust faults, the Lower Southern Thrust and the Upper Northern Thrust. The bulk displacement of these faults is towards the south. Both faults have a general E-W trend. Meanwhile, the study area comprises three asymmetrical anticlines. From east to west, these are the Ora, Harur, and Nazdur (Figure 1).

3. Sampling and methods

The samples were collected from 2 sections: Sararu and Nazdur. The former lies along the southern limb of the Ora anticline whereas the latter is found at the northern flank of the Nazdur anticline (Figure 1). A total of 42 shale samples were collected from the Beduh Formation (21 samples from each section) and washed thoroughly to remove contamination. Samples were crushed into small pieces and further separated into grain sizes of less than 200 mesh by standardized dry sieving.

The clay mineralogy of 12 shale samples (6 from each section) was determined by conventional X-ray diffraction (XRD) method using a Philips PM8203 X-ray diffractometer with Ni-filtered CuKα radiation using 40 kV and 40 mA at the X-ray laboratories of the Iraqi Geological Survey, Baghdad, Iraq. The samples were X-rayed using a scan range from 3° to 50° 2θ for the crushed bulk samples and from 3° to 20° 2θ for the clay fraction at an interval of 0.02° 2θ per second using a rotating sample holder. The clay fraction (<2 μm) was separated out from the shale by disaggregating and dispersing the sample in distilled water by pipette method, and oriented slides were prepared to obtain a good reflection (Friedman and Johnson, 1982). The clay samples in oriented mounts were run under three separate conditions: air-dried state, after ethylene glycol treatment at 25 °C for 15 h, and after heating to 550 °C for 1 h. For the semiquantitative analysis, peak areas of the specific reflections of the main clay minerals were calculated (Grim, 1968; Carroll, 1970).

The 42 samples were analyzed for major elements, trace elements, and REE geochemistry. Chemical analyses were performed at Acme Analytical Laboratories, Vancouver, Canada. Major and some trace element (Cr, Cu, Pb, Zn, and Ni) concentrations were analyzed by X-ray fluorescence spectrometry under the analysis code 4X. Loss on ignition (LOI) was determined from the total weight after ignition at 1000 °C for 2 h. Other trace and REE concentrations were measured by inductively coupled plasma mass spectrometer under the code 4B; all samples were fused with $LiBO_2$ followed by treatment with HNO_3. Chemical analysis for major elements has precision of better than 2%, whereas for the trace elements and REEs precision varies between 1% and 10%. Internationally recognized standard materials OREAS72B, SO-18, and OREAS45EA were used as references. Based on these standards, the accuracy and the precision of the analyses were within ±2% for elements like Zn, Rb, V, Zr, Y, La, Sm, Tb, Dy, Tm, Yb, and Lu; ±5% for Ni, Cu, Cr, Co, and Eu; and ±10% for Hf, Ta, W, and Er.

The post-Archean Australian shale (PAAS) values were used for comparison. The REE data were normalized to the chondrite values of Taylor and McLennan (1985). The normalized Eu anomaly (Eu/Eu*) was calculated by the following equation: $Eu/Eu^{\star} = Eu_n/(Sm_n \times Gd_n)^{1/2}$, where the subscript n denotes chondrite normalized values (Taylor and McLennan, 1985).

The chemical index of alteration (CIA) and chemical index of weathering (CIW) were calculated following the methods of Nesbitt and Young (1982) and Harnois (1988), respectively. CaO was corrected by the method of McLennan et al. (1993), whereby CaO values were accepted only if $CaO < Na_2O$; when $CaO > Na_2O$, it was assumed that the concentration of CaO equaled that of Na_2O.

4. Results

4.1. Mineralogy

XRD analysis of selected shale samples from the Beduh Formation indicates that clay minerals are mainly represented by illite and kaolinite, with minor amounts of chlorite and a mixed layer (illite/smectite and illite/chlorite). On the other hand, calcites and quartz together with small amounts of albitic feldspar and hematite are the dominant nonclay species (Figure 5). Identification of secondary minerals was difficult because their peaks tended to be obscured by the greater peaks of the major minerals. The analysis revealed obvious qualitative differences in bulk mineral compositions among the shale samples (Table 1). Illite varies from 38.3% to 77.5% with an average of 55.03% while kaolinite ranges from 5.9% to 44.1% with an average value of 26.54%. The samples generally showed moderate values of the Kübler (illite) crystallinity index, ranging between 0.41° and 0.70° Δ2θ with an average of 0.52° Δ2θ (Table 1). This index was determined by measuring the half-peak width of the 10 Å illite on oriented mineral aggregate preparations of the <2 μm size fractions and is expressed in °Δ2θ (Kübler, 1967). All the studied samples have illite chemistry index (5 Å/10 Å ratios) of >0.4 (Table 1; Figure 6).

4.2. Geochemistry

4.2.1. Major element geochemistry

The major element concentrations of the Beduh Formation are given in Table 2. In general, the shale of the Beduh Formation has high CaO content (3.43%–38.13%, avg.

a

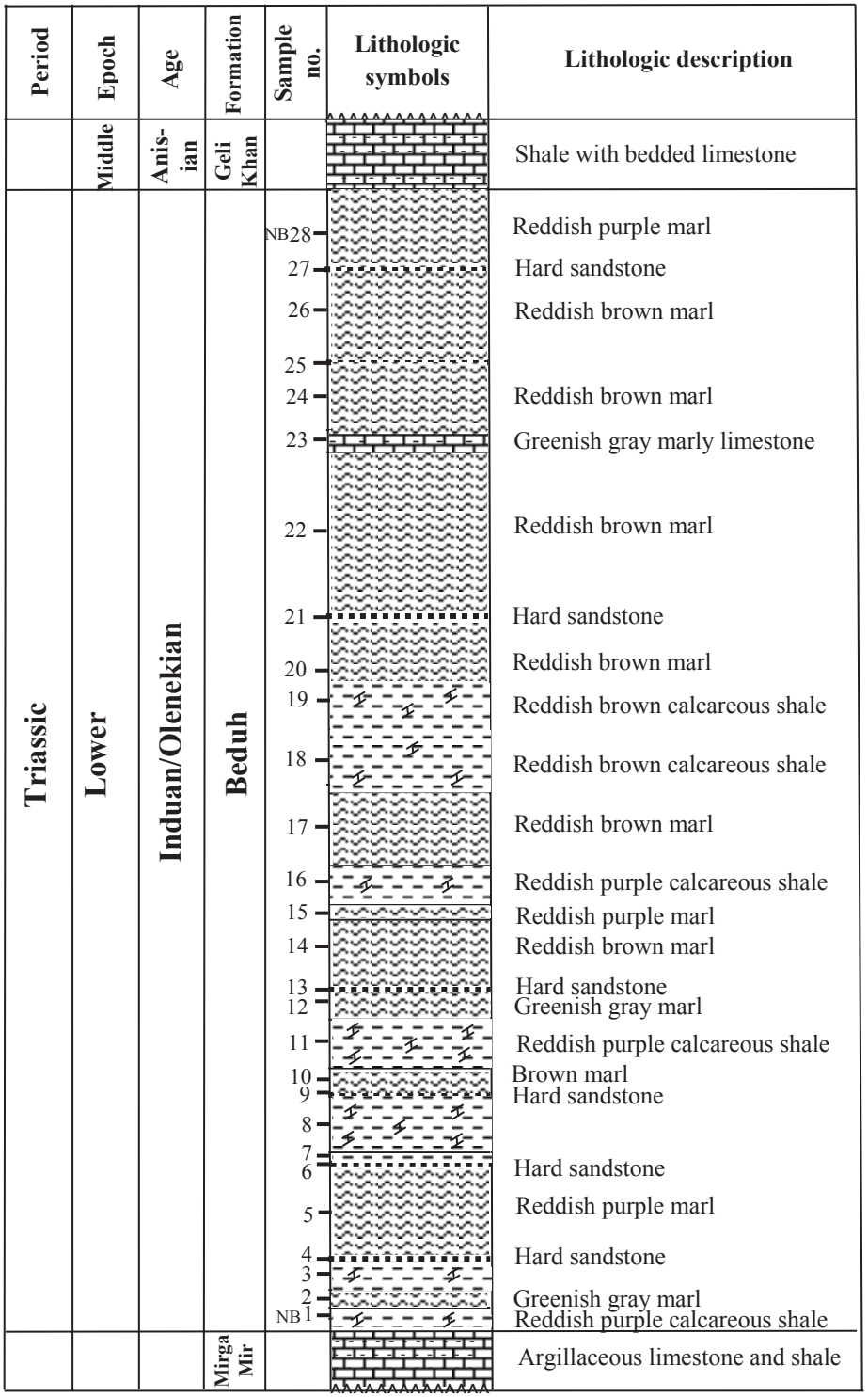

Figure 4. Columnar sections of the Beduh Formation: a) Nazdur section, b) Sararu section.

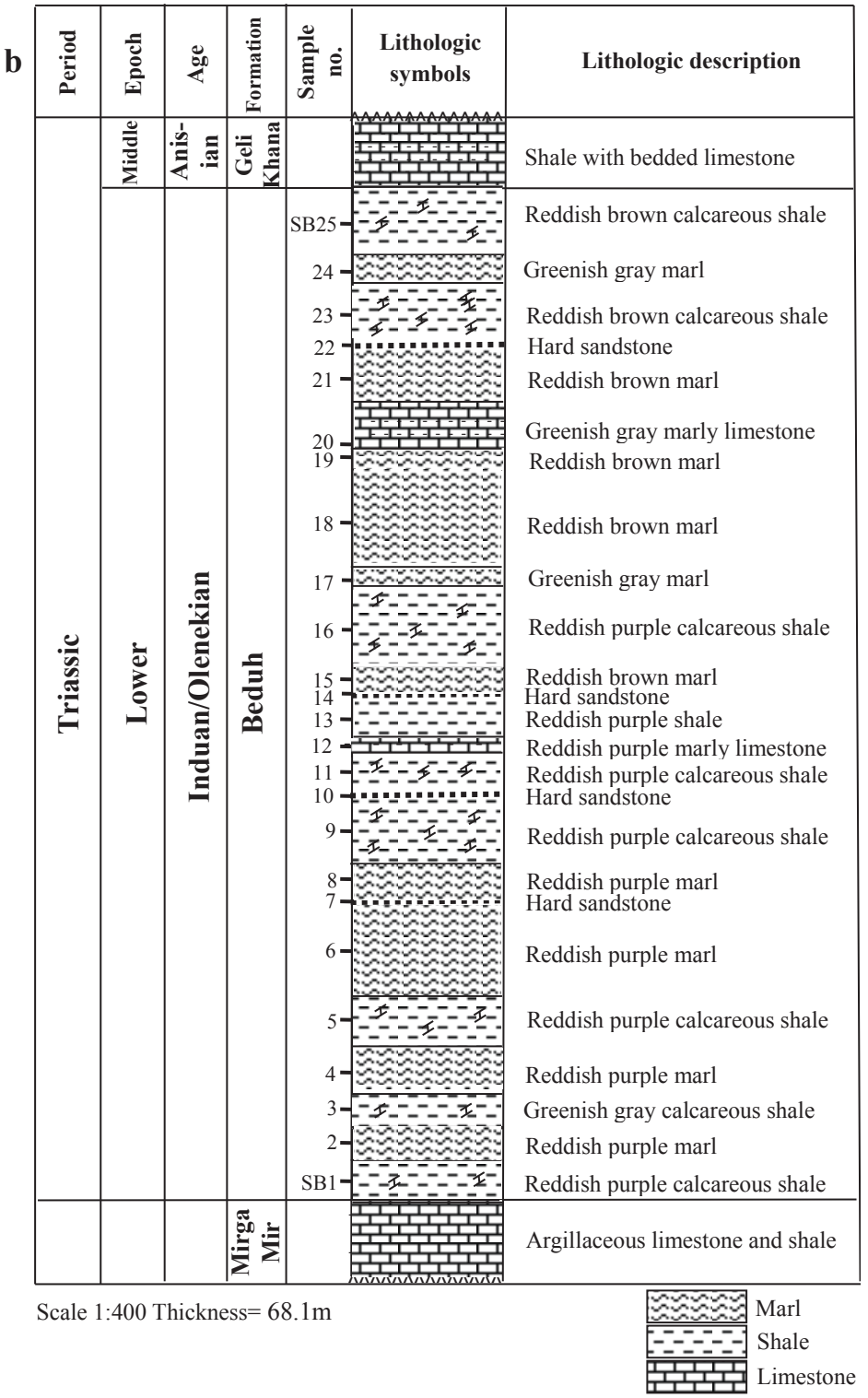

Figure 4. Columnar sections of the Beduh Formation: a) Nazdur section, b) Sararu section.

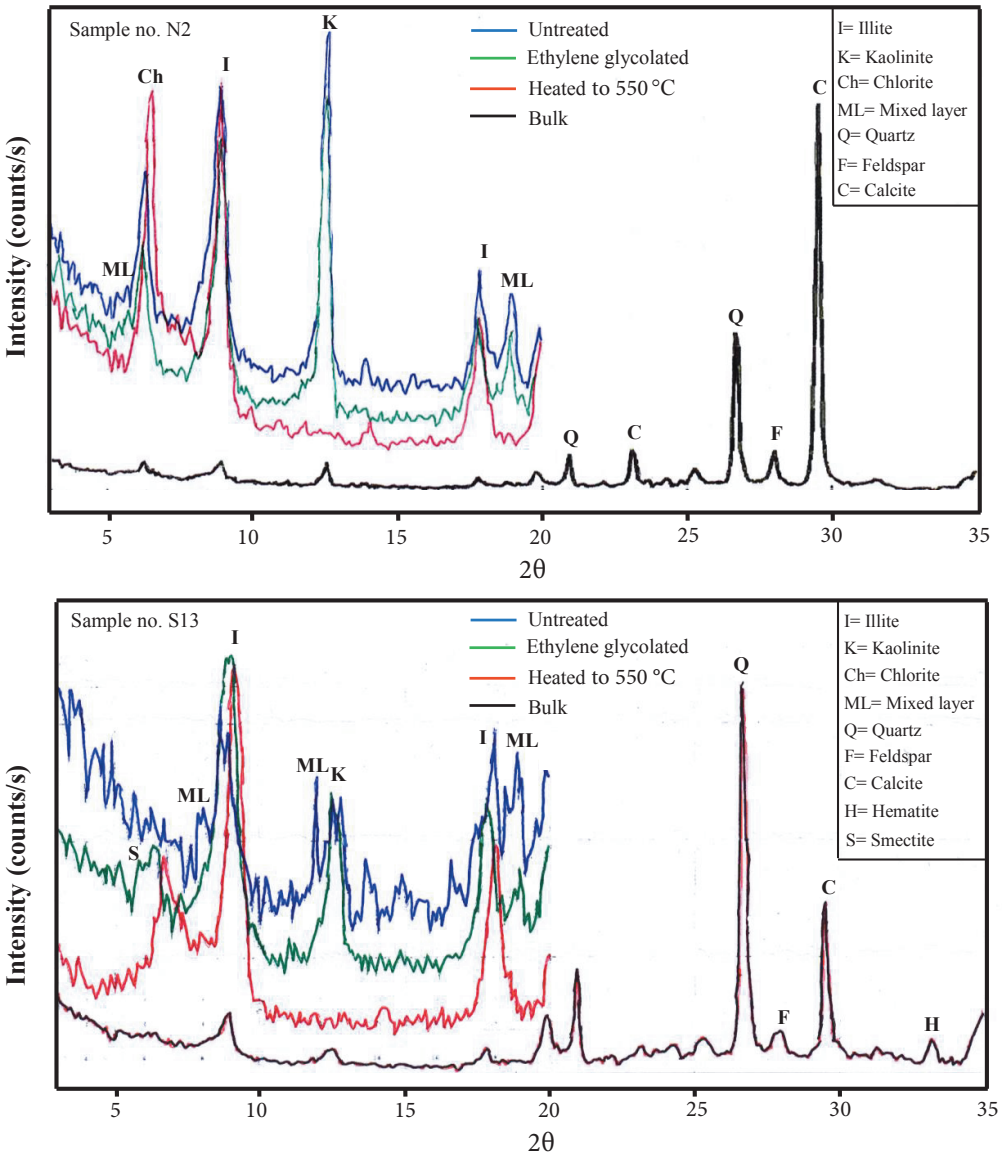

Figure 5. X-ray diffractograms for selected shale samples from the Nazdur and Sararu sections.

= 22.0%). Such content has a great dilution effect on the other oxides, i.e. SiO_2 content (19.46%–54.37%, avg. = 36.38%), Al_2O_3 (5.80%–19.11%, avg. = 11.37%), TiO_2 (0.27%–0.69%, avg. = 0.46%), K_2O (1.07%–4.72%, avg. = 3.68%), and Na_2O (0.29%–0.99%, avg. = 0.61). Except for CaO, the studied shale shows depletion in all elements relative to those of the PAAS (Table 2). The enrichment of CaO in these samples, as well as the significant correlation between CaO and LOI (r = 0.999, n = 42), suggest that LOI and CaO are incorporated into calcite rather than other elements. On the other hand, Al_2O_3 shows positive correlations with SiO_2, Fe_2O_3, K_2O, MgO, TiO_2, and P_2O_5 (r = 0.920, 0.983, 0.998, 0.917, 0.956, and 0.675, respectively; Table 3).

4.2.2. Trace element geochemistry

The trace element contents of the Beduh Formation are reported in Table 4. The studied samples show enrichment of Sr and depletion in Ba, Co, Rb, Th, U, Y, Cr, and Ni relative to PAAS (Table 4). The enrichment of Sr (42.8–1012, avg. = 418 ppm) in a few samples is probably linked to the carbonate content (Yan et al., 2007). This is consistent with the significant positive correlation between CaO and Sr (r = 0.871). Al_2O_3 is positively correlated with HFSEs such as Th, Y, and Nb (r = 0.908, 0.741, and 0.934, respectively; n = 42; Table 3), and LILEs such as Rb (r = 0.977; n = 42; Table 3), suggesting that these elements may be bound in clay minerals and concentrated during weathering (Fedo et al., 1996; Nagarajan et al., 2007). In addition,

Table 1. Mineralogical composition and crystallographic parameters of the calcareous shale from the Beduh Formation.

Sample no.	Nonclay minerals					Clay minerals							
	Calcite %	Quartz %	Feldspar %	Muscovite %	Hematite %	Illite %	Kaolinite %	Chlorite %	Mixed layer %	Illite chemistry index	Illite crystallinity index (mm)	Illite crystallinity index (2θ)	Kaolinite crystallinity index
N23	83.1	14.2	2.7	-	-	38.3	42.4	19.3		0.82	8.4	0.50	0.030
N22	63.5	31.7	2.1	1.9	0.8	54.9	18.8		34.3[1]	0.56	8.5	0.70	0.210
N16	6.6	82.9	6.3	3.8	0.4	69.7	14.9		15.4[2]	0.56	8.5	0.61	0.060
N14	70.6	27.3	0.9	0.5	0.7	54.3	12.3		33.4[1]	0.41	6.7	0.50	0.210
N3	36.3	54.9	3.6	3.3	1.9	50.6	36.7	12.7		0.45	9.1	0.50	0.030
N2	76.4	17.8	4.1	1.7	-	44.2	37.1	18.7		0.42	7.0	0.52	0.023
S25	30.9	60.9	1.4	4.3	2.5	77.5	5.9		16.6[2]	0.52	5.1	0.41	0.210
S20	85.0	13.1	1.4	0.5	-	50.1	44.1	5.8		0.64	8.4	0.52	0.037
S19	65.0	28.6	4.8	1.6	-	57.8	28.9	13.3		0.44	7.5	0.58	0.030
S13	29.8	59.0	2.0	6.6	2.6	53.4	24.0		22.6[1]	0.92	6.8	0.52	0.080
S5	50.9	40.8	3.8	3.1	1.4	57.2	19.3		23.5[1]	0.59	8.0	0.50	0.036
S4	64.9	29.6	3.2	2.3	-	52.4	34.1	13.5		0.51	5.5	0.42	0.026
Average	55.25	38.40	3.03	2.69	1.47	55.03	26.54	13.88	24.31	0.57	7.46	0.52	0.08

Note: Clay minerals represent 100% and nonclay represent 100%.
[1] Illite/chlorite mixed layer.
[2] Illite/smectite mixed layer.
N = Nazdur section.
S = Sararu section.

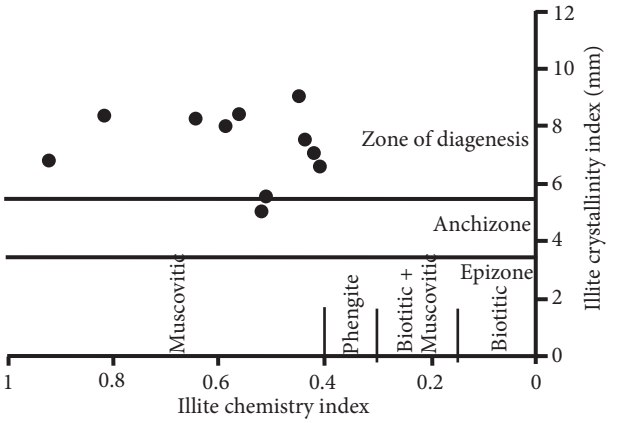

Figure 6. Relationship between illite crystallinity indices (after Esquevin, 1969); anchizone limits after Dunoyer de Segonzac (1969).

Al_2O_3 positively correlated with most of the transitional elements (TTEs) such as Co, V, and Zn (r = 0.932, 0.969, and 0.960, respectively; n = 42; Table 3), indicating their incorporation in clay minerals.

The Zr, Hf, and Nb contents are depleted compared with PAAS. Th and U behave differently during weathering and sedimentary recycling as the latter is chemically mobile, which leads to decrease in the U/Th ratio. In the present rock samples, the U/Th ratio varies from 0.17 to 0.38 with an average of 0.27, which is higher than PAAS value of 0.21 (Table 4).

4.2.3. Rare earth elements

The content of total rare earth elements (ΣREE) varies from 91.22 to 213.43 ppm with an average of 146.40 ppm, lower than for the PAAS (184.77 ppm; Table 5). The results suggest that the major control over the REE concentrations is the dilution effect caused by carbonate (correlation coefficient between CaO and ΣREE is –0.875). In this regard, the significant correlations of ΣREE with Al_2O_3 and K_2O (Table 3) suggest that clay minerals typically control REE distribution in shales (McLennan, 1989; Condie, 1991). The chondrite normalized (Taylor and McLennan, 1985) REE patterns of these samples (Figure 7) are uniform, indicating that they have a similar source. Beduh shale exhibits REE fractionation with $(La/Yb)_n$ = 8.97 and negative Eu anomaly (Eu/Eu* = 0.72), which is attributed to the Eu-depleted felsic igneous rocks in the source area (Figure 7).

5. Discussion

5.1. Clay mineralogy

The moderate values of the illite crystallinity index indicate a moderate-grade chemical degradation in the source area during transportation and sedimentation. The illite crystallinity of the marine sediments is higher than that of the fluvial deposits. This can be explained by the capacity of illite in the marine environment to fix new ions available in seawater (Millot, 1964), since Fe and Mg tend to be replaced by K and Al, increasing illite crystallinity (Nemecz, 1981; Oliveira et al., 2002). According to the illite crystallinity index most of the studied samples plotted in the zone of diagenesis. All the studied samples have an Esquevin index (illite chemistry index) value of >0.4 (Table 1; Figure 6), corresponding to Al-rich illite (muscovite type) reflecting a granitic provenance. The kaolinite has a low crystallinity index, i.e. high crystallinity, which can be explained by being directly supplied from the rivers (Oliveira et al., 2002).

The significant positive correlation between kaolinite content and illite crystallinity index (r = 0.92; n = 12) reflects the higher kaolinite content corresponding to lower illite crystallinity (Table 6), whereas the significant negative relationship between kaolinite content and kaolinite crystallinity index (r = –0.98; n = 12) reflects the higher kaolinite proportion corresponding to the higher kaolinite crystallinity. Similarly, the positive significant correlation between illite content and kaolinite crystallinity index (r = 0.74; n = 12) reflects the higher illite content corresponding to lower kaolinite crystallinity, while the negative significant correlation between illite content and its crystallinity index (r = –0.694; n = 12) reflects the higher illite proportion corresponding to higher illite crystallinity, i.e. a well-ordered structure.

5.2. Source area weathering

The rate of chemical weathering of source rocks and the erosion rate of weathering profiles are controlled by climate as well as source rock composition and tectonics; warm humid climate and stable tectonic settings favor chemical weathering. Absence of chemical alteration results in low CIA values, which may reflect cool and/or arid conditions or alternatively rapid physical weathering and erosion under an active tectonic setting (Fedo et al., 1995; Nesbitt et al., 1997; Singh, 2009, 2010; Absar and Sreenivas, 2015; Tawfik et al., 2015). Fresh igneous rocks and minerals have CIA values of 50 or less (Nesbitt and Young, 1982).

The intensity of weathering in clastic sediments in the source area can be evaluated by examining the relationships between alkali and alkaline earth elements (Nesbitt and Young, 1996; Nesbitt et al., 1997). This can be deduced through the calculated values of the CIA and CIW, which are defined as follows:

$CIA = [Al_2O_3 / (Al_2O_3+CaO^*+Na_2O+K_2O)] \times 100$ (Nesbitt and Young, 1982),

$CIW = [Al_2O_3 / (Al_2O_3+CaO^*+Na_2O)] \times 100$ (Harnois, 1988),

where the oxides are expressed as molar proportions and CaO^* represent the Ca in silicate fractions only. The CIA values of shale range between 71 and 78 with an

Table 2. Major element data (wt.%) of calcareous shale from the Beduh Formation.

	N1	N2	N3	N5	N7	N8	N10	N11	N12	N14	N15	N16	N17	N18	N19
SiO_2	54.37	28.52	42.68	36.16	47.09	46.08	31.87	50.86	44.97	30.83	27.39	53.88	31.19	39.98	40.07
Al_2O_3	17.97	8.91	14.44	12.21	11.68	15.87	10.16	16.51	8.58	10.79	8.61	19.11	8.08	13.33	13.33
Fe_2O_3	6.97	3.58	6.75	4.88	3.88	6.55	3.9	6.54	3.11	4.13	3.06	7.63	2.92	5.45	5.46
CaO	4.58	28.62	14.04	20.97	15.91	11.12	26.07	8.03	20.65	26.05	30.66	3.43	28.8	17.41	17.52
MgO	2.62	1.74	2.32	1.93	1.74	2.14	1.56	2.12	1.14	1.37	1.24	2.05	1.27	1.64	1.65
Na_2O	0.64	0.76	0.76	0.67	0.65	0.59	0.59	0.81	0.99	0.44	0.57	0.52	0.74	0.51	0.52
K_2O	4.35	1.77	3.38	2.79	2.64	3.78	2.21	3.91	1.68	2.48	1.82	4.72	1.57	3.14	3.12
MnO	0.02	0.05	0.05	0.05	0.08	0.05	0.06	0.04	0.06	0.05	0.06	0.02	0.06	0.05	0.05
TiO_2	0.64	0.37	0.5	0.43	0.48	0.58	0.4	0.63	0.52	0.4	0.36	0.69	0.36	0.51	0.51
P_2O_5	0.12	0.07	0.09	0.08	0.15	0.12	0.08	0.12	0.12	0.07	0.06	0.13	0.08	0.1	0.1
LOI	8.73	25.3	14.94	19.79	15.61	13.15	23.24	10.67	18.29	23.56	26.39	7.88	24.85	17.59	17.62
Total	101.07	99.73	99.99	99.99	100	100.07	100.16	100.3	100.16	100.22	100.26	100.12	99.95	99.74	99.98
CIA	76.34	73.48	74.95	75.02	75.08	76.40	75.30	75.18	70.65	76.48	74.77	77.00	73.07	76.43	76.43
CIW	93.65	86.03	90.90	90.54	90.42	93.39	90.05	91.46	81.99	92.80	88.81	95.08	85.16	93.21	93.09
SiO_2/Al_2O_3	3.03	3.2	2.96	2.96	4.03	2.9	3.14	3.08	5.24	2.86	3.18	2.82	3.86	3	3.01
Al_2O_3/TiO_2	28.08	24.08	28.88	28.4	24.33	27.36	25.4	26.21	16.5	26.98	23.92	27.7	22.44	26.14	26.14
K_2O/Na_2O	6.8	2.33	4.45	4.16	4.06	6.41	3.75	4.83	1.7	5.64	3.19	9.08	2.12	6.16	6
K_2O/Al_2O_3	0.24	0.2	0.23	0.23	0.23	0.24	0.22	0.24	0.2	0.23	0.21	0.25	0.19	0.24	0.23

Table 2. (Continued).

	N20	N22	N23	N24	N26	N28	S1	S2	S3	S4	S5	S6	S8	S9	S11
SiO_2	24.58	33.99	24.81	34.23	33.59	35.75	51.05	33.66	46.82	32.41	40.93	28.42	33.13	47.52	40.32
Al_2O_3	7.61	10.13	6.25	10.63	9.47	11.18	17.33	10.05	14.27	10.35	13.59	8	11.51	13.79	12.78
Fe_2O_3	2.54	4.03	2.37	4.47	3.78	4.51	6.5	3.68	6.19	3.6	5.19	2.85	4.07	5.2	5.47
CaO	33.17	24.79	34.36	23.77	25.46	22.33	7.39	25.2	12.21	25.63	17.09	30.66	23.93	13.28	17.93
MgO	1.12	1.33	1.14	1.51	1.32	1.5	2.09	1.43	2.1	1.52	1.74	1.21	1.48	1.89	1.85
Na_2O	0.53	0.64	0.64	0.55	0.7	0.71	0.65	0.73	0.88	0.62	0.57	0.62	0.49	0.77	0.66
K_2O	1.61	2.16	1.22	2.46	2.11	2.56	4.26	2.14	3.21	2.19	3.23	1.62	2.64	3.18	3.01
MnO	0.05	0.05	0.07	0.05	0.05	0.04	0.05	0.06	0.05	0.05	0.04	0.06	0.05	0.06	0.05
TiO_2	0.32	0.47	0.32	0.44	0.42	0.49	0.64	0.44	0.56	0.41	0.51	0.35	0.43	0.54	0.51
P_2O_5	0.06	0.12	0.09	0.09	0.1	0.11	0.12	0.08	0.11	0.08	0.11	0.07	0.07	0.1	0.1
LOI	28.22	22.3	28.8	21.82	22.64	20.56	10.29	22.52	13.3	22.91	16.96	26.21	22.09	14.05	17.52
Total	99.84	100.05	100.1	100.04	99.68	99.77	100.42	100.02	99.75	99.81	99.99	100.12	99.92	100.41	100.23
CIA	74.40	74.99	71.94	75.19	73.34	74.08	75.92	74.01	74.50	75.44	75.90	74.07	76.31	74.80	74.97
CIW	88.30	89.27	83.69	91.04	87.67	89.22	93.34	87.85	89.50	89.77	92.61	87.15	92.50	90.39	91.05
SiO_2/Al_2O_3	3.23	3.36	3.97	3.22	3.55	3.2	2.95	3.35	3.28	3.13	3.01	3.55	2.88	3.45	3.15
Al_2O_3/TiO_2	23.78	21.55	19.53	24.16	22.55	22.82	27.08	22.84	25.48	25.24	26.65	22.86	26.77	25.54	25.06
K_2O/Na_2O	3.04	3.38	1.91	4.47	3.01	3.61	6.55	2.93	3.65	3.53	5.67	2.61	5.39	4.13	4.56
K_2O/Al_2O_3	0.21	0.21	0.2	0.23	0.22	0.23	0.25	0.21	0.22	0.21	0.24	0.2	0.23	0.23	0.24

Table 2. (Continued).

	S12	S13	S15	S16	S17	S18	S19	S20	S21	S23	S24	S25	Average	PAAS
SiO_2	21.61	49.59	24.28	37.88	28.22	32.51	29.05	19.46	26.15	41.28	24.34	46.43	36.38	62.4
Al_2O_3	6.5	17.52	7.52	13.18	5.8	11.18	7.96	5.99	8.33	13.44	6.96	16.59	11.37	18.78
Fe_2O_3	2.34	7.08	2.52	5.57	1.95	4.28	3.02	2.01	3.21	5.39	2.43	6.97	4.43	7.18
CaO	35.48	7.48	33.46	19.19	32.7	24.42	29.98	38.13	31.31	16.8	34.02	9.99	22	1.29
MgO	1.07	2.2	1.16	1.73	1.07	1.5	1.24	1.19	1.23	1.68	1.13	1.89	1.59	2.19
Na_2O	0.51	0.56	0.5	0.47	0.65	0.47	0.75	0.42	0.45	0.46	0.54	0.29	0.61	1.19
K_2O	1.32	4.3	1.53	3.19	1.07	2.55	1.62	1.15	1.81	3.23	1.42	4.14	2.58	3.68
MnO	0.06	0.04	0.05	0.04	0.07	0.04	0.05	0.05	0.05	0.04	0.04	0.04	0.05	0.11
TiO_2	0.27	0.62	0.32	0.5	0.3	0.45	0.39	0.29	0.35	0.52	0.32	0.62	0.46	0.99
P_2O_5	0.05	0.12	0.06	0.1	0.09	0.1	0.11	0.07	0.08	0.12	0.07	0.12	0.1	0.16
LOI	30.05	10.36	28.46	18.77	27.67	22.46	25.63	31.53	27.16	17.16	28.87	12.97	20.45	6
Total	99.28	99.91	99.88	100.65	99.63	99.98	99.87	100.33	100.15	100.17	100.17	100.09	100.05	103.97
CIA	73.94	76.55	75.19	76.34	71.54	76.45	72.31	75.45	75.75	76.60	73.98	77.95	74.96	75.4
CIW	87.01	94.27	88.77	93.64	82.42	92.59	84.79	88.23	90.68	93.88	87.13	96.78	90.00	90.56
SiO_2/Al_2O_3	3.32	2.83	3.23	2.87	4.87	2.91	3.65	3.25	3.14	3.07	3.5	2.8	3.29	3.32
Al_2O_3/TiO_2	24.07	28.26	23.5	26.36	19.33	24.84	20.41	20.66	23.8	25.85	21.75	26.76	24.53	19
K_2O/Na_2O	2.59	7.68	3.06	6.79	1.65	5.45	2.16	2.74	4.02	7.02	2.63	14.28	4.5	3.09
K_2O/Al_2O_3	0.2	0.25	0.2	0.24	0.18	0.23	0.2	0.19	0.22	0.24	0.2	0.25	0.22	0.2

average value of 75, similar to the PAAS value (Table 2; Figure 8), indicating a moderate to high degree of chemical weathering. Nesbitt et al. (1997) illustrated that the CIA values may also be influenced by tectonism. Meanwhile, the restricted CIA values are typical of steady-state weathering conditions, which probably indicates the absence of active tectonism in the Arabian Plate during the Lower Triassic.

The CIA values are also plotted on the Al_2O_3 - (CaO^*+Na_2O) - K_2O (A-CN-K) diagram (Figure 8) in order to evaluate the extent of weathering history of igneous rocks (Nesbitt and Young, 1984) and K-metasomatism (Fedo et al., 1995), where unweathered rocks plot along the plagioclase-K-feldspar line (Nesbitt and Young, 1984). In the A-CN-K diagram, the shale of the Beduh Formation forms a weathering trend that is almost perpendicular to the A-K line close to the illite composition, indicating an intense chemical weathering of the source rocks and suggestive of K-enrichment during diagenesis. The samples plot away from the K-feldspar-plagioclase line and the elevated CIA values may reflect the higher proportion of clay minerals than feldspars.

When postdepositional K-metasomatism occurs, the weathering trend line deviates from the predicted weathering line and moves towards the K_2O apex (Figure 8, dashed line with arrow). On the A-CN-K plot (Figure 8), the Beduh shale shows a deviation trend line from the predicted weathering trend. The premetasomatized CIA values of the studied shale can be estimated by drawing a line from the K_2O apex through an individual CIA data point; the intersection point of this line with the 'predicted weathering line' provides the premetasomatism CIA values (Bhat and Ghosh, 2001; Tao et al., 2014). The premetasomatism CIA values of the shales range between 72.5 and 88.0 with an average of 80.25, indicating moderate to intense weathering in the source area.

Harnois (1988) proposed the CIW index to monitor paleoweathering at the source area, which is not sensitive to postdepositional K enrichments. The shale of the Beduh Formation possesses CIW values ranging from 81.96 to 96.78, similar to the PAAS value (Table 2). However, Tawfik et al. (2015) suggested that the high values could reflect a prolonged dissolution of unstable plagioclases during transportation and/or diagenesis, rather than extreme chemical weathering at the source terrain.

Th/U in sedimentary rocks is of interest, as weathering and recycling typically result in loss of U, leading to an increase in the Th/U ratio. The Th/U ratio in most upper crustal rocks varies between 3.5 and 4.0 (McLennan et al., 1993). In sedimentary rocks, Th/U values higher than 4.0 may indicate intense weathering in source areas or sediment recycling. Th/U ratios in the Beduh shale range from 2.61 to 5.83 with an average of 3.90 (Table 4), indicating a moderate weathering intensity in the source area.

Table 3. Correlation matrix for the calcareous shale from the Beduh Formation.

	SiO_2	Al_2O_3	Fe_2O_3	CaO	MgO	Na_2O	K_2O	MnO	TiO_2	P_2O_5	LOI	Ba	Co	Cs	Hf	Nb	Rb	Sr	Th	U	V	Zr	Y	Cu	Cr	Pb	Zn	Ni	REE
SiO_2	1																												
Al_2O_3	**0.920**	1																											
Fe_2O_3	**0.890**	**0.983**	1																										
CaO	**−0.983**	**−0.975**	**−0.955**	1																									
MgO	**0.853**	**0.917**	**0.922**	**−0.904**	1																								
Na_2O	0.259	−0.019	−0.004	−0.145	0.142	1																							
K_2O	**0.904**	**0.998**	**0.981**	**−0.964**	**0.903**	−0.074	1																						
MnO	−0.393	**−0.593**	**−0.599**	**0.490**	**−0.499**	0.271	**−0.606**	1																					
TiO_2	**0.966**	**0.956**	**0.938**	**−0.981**	**0.843**	0.138	**0.947**	**−0.541**	1																				
P_2O_5	**0.822**	**0.675**	**0.652**	**−0.772**	**0.580**	0.220	**0.667**	−0.253	**0.804**	1																			
LOI	**−0.990**	**−0.964**	**−0.943**	**0.999**	**−0.897**	−0.186	**−0.952**	**0.465**	**−0.980**	**−0.785**	1																		
Ba	0.306	0.173	0.112	−0.242	0.155	0.168	0.159	0.117	0.245	**0.458**	−0.261	1																	
Co	**0.871**	**0.932**	**0.933**	**−0.921**	**0.899**	0.031	**0.926**	**−0.414**	**0.886**	**0.667**	**−0.914**	0.182	1																
Cs	**0.911**	**0.981**	**0.959**	**−0.960**	**0.896**	−0.046	**0.983**	**−0.578**	**0.938**	**0.693**	**−0.950**	0.240	**0.919**	1															
Hf	**0.767**	**0.579**	**0.572**	**−0.698**	**0.463**	0.366	**0.565**	−0.260	**0.728**	**0.651**	**−0.717**	0.237	**0.517**	**0.570**	1														
Nb	**0.938**	**0.934**	**0.929**	**−0.957**	**0.847**	0.141	**0.925**	**−0.487**	**0.958**	**0.763**	**−0.957**	0.173	**0.901**	**0.915**	**0.700**	1													
Rb	**0.865**	**0.977**	**0.971**	**−0.934**	**0.885**	−0.130	**0.983**	**−0.618**	**0.917**	**0.633**	**−0.919**	0.104	**0.926**	**0.963**	**0.556**	**0.924**	1												
Sr	**−0.873**	**−0.815**	**−0.831**	**0.871**	**−0.804**	−0.256	**−0.804**	0.341	**−0.862**	**−0.806**	**0.874**	−0.233	**−0.767**	**−0.792**	**−0.641**	**−0.851**	**−0.760**	1											
Th	**0.876**	**0.908**	**0.894**	**−0.909**	**0.832**	0.084	**0.904**	**−0.549**	**0.932**	**0.811**	**−0.904**	0.302	**0.841**	**0.913**	**0.527**	**0.880**	**0.864**	**−0.843**	1										
U	**0.516**	**0.503**	**0.437**	**−0.513**	0.388	−0.086	**0.506**	−0.191	**0.547**	**0.622**	**−0.509**	**0.514**	**0.440**	**0.536**	0.203	**0.427**	**0.447**	**−0.500**	**0.656**	1									
V	**0.908**	**0.969**	**0.945**	**−0.954**	**0.909**	0.024	**0.963**	**−0.532**	**0.930**	**0.666**	**−0.944**	0.218	**0.890**	**0.948**	**0.547**	**0.904**	**0.925**	**−0.829**	**0.893**	**0.505**	1								
Zr	**0.785**	**0.586**	**0.576**	**−0.710**	**0.444**	0.374	**0.570**	−0.239	**0.760**	**0.724**	**−0.730**	0.255	**0.530**	**0.574**	**0.960**	**0.730**	**0.554**	**−0.673**	**0.569**	0.281	**0.568**	1							
Y	**0.777**	**0.741**	**0.772**	**−0.782**	**0.647**	0.222	**0.733**	**−0.405**	**0.836**	**0.831**	**−0.788**	0.245	**0.705**	**0.729**	**0.616**	**0.830**	**0.725**	**−0.791**	**0.862**	**0.485**	**0.715**	**0.674**	1						
Cu	−0.224	−0.301	−0.344	0.267	−0.189	0.099	−0.308	**0.436**	−0.320	−0.175	0.258	0.019	−0.243	−0.277	−0.298	−0.346	−0.336	0.152	−0.290	0.018	−0.260	−0.306	−0.295	1					
Cr	0.381	0.292	0.210	−0.334	0.176	0.108	0.278	−0.169	0.365	0.282	−0.342	0.122	0.227	0.263	0.267	0.233	0.214	−0.205	0.261	0.296	0.294	0.289	0.078	−0.015	1				
Pb	**0.619**	**0.544**	**0.567**	**−0.601**	0.334	−0.012	**0.555**	−0.268	**0.677**	**0.785**	**−0.606**	0.223	**0.532**	**0.559**	**0.642**	**0.677**	**0.571**	**−0.644**	**0.614**	0.365	**0.527**	**0.718**	**0.758**	−0.359	0.182	1			
Zn	**0.881**	**0.960**	**0.965**	**−0.940**	**0.926**	0.046	**0.952**	**−0.510**	**0.910**	**0.663**	**−0.930**	0.144	**0.957**	**0.932**	**0.504**	**0.892**	**0.927**	**−0.812**	**0.884**	**0.476**	**0.928**	**0.515**	**0.747**	−0.244	0.242	**0.509**	1		
Ni	**0.888**	**0.964**	**0.968**	**−0.944**	**0.878**	−0.020	**0.962**	**−0.565**	**0.933**	**0.705**	**−0.933**	0.177	**0.929**	**0.949**	**0.555**	**0.919**	**0.941**	**−0.837**	**0.903**	**0.503**	**0.935**	**0.578**	**0.772**	−0.330	0.263	**0.608***	**0.965**	1	
REE	**0.842**	**0.870**	**0.879**	**−0.875**	**0.803**	0.080	**0.868**	**−0.515**	**0.899**	**0.832**	**−0.871**	0.301	**0.844**	**0.882**	**0.498**	**0.873**	**0.846**	**−0.841**	**0.972**	**0.619**	**0.841**	**0.547**	**0.903**	−0.269	0.212	**0.672**	**0.870**	**0.891**	1

Underlined: Significant at 0.05 level.
Bolded: Significant at 0.01 level.
No. of samples = 42.

Table 4. Trace element concentrations (ppm) of calcareous shale from the Beduh Formation, compared with PAAS (Taylor and McLennan, 1985.

	N1	N2	N3	N5	N7	N8	N10	N11	N12	N14	N15	N16	N17	N18	N19
Ba	311	151	203	241	495	258	192	320	292	183	232	356	276	253	220
Co	11.7	8.6	13.7	11.7	12.4	15.6	9.7	14.6	7.8	8.1	7.5	13.8	6.9	11.5	11
Cs	10.9	2.9	7.9	7.3	7.3	8	5	10.4	3.6	4.6	3.8	12.1	3.4	7.4	6.7
Hf	3.3	2.2	3.2	2.3	2.8	2.8	1.9	3	5.3	1.9	2.1	4	2.3	2.9	3
Nb	11.9	7.8	10.9	9.5	10.3	11.1	8.5	11.8	9.5	7.6	6.9	14.5	6.8	10.6	11.5
Rb	155.4	64.6	130.5	109	91	135.3	83.5	132.6	61.4	86.5	70	168	56.1	113.7	124.7
Sr	91.5	401.9	180.8	303	242.4	213.6	541.4	154.8	342.7	424.9	724.5	124	540.4	263.2	297.2
Th	17.3	7.9	12.1	10	12.3	14.4	9	16.4	8.4	8.9	8.1	16.7	7.9	12.7	11
U	3.4	2.3	2.3	2.3	3.3	3.2	2.4	3.3	2.4	2.8	2.7	3.3	2.8	2.9	2.6
V	119	60	89	82	83	93	63	97	55	71	51	113	50	85	77
Zr	114.1	77	99.2	86.3	104.2	104.4	83.6	112.5	188.5	73	76.4	143.1	87	108.2	114.2
Y	25.4	14.2	25.1	19.4	21.3	25.7	19.1	26.1	23	15.4	16.3	29.2	15	22.5	25.1
Cu	13.8	32.9	8.6	23.1	42.9	14.8	50.6	53.1	13.4	13.9	33	2.4	16.7	3.9	3.3
Cr	58.1	27.4	30.8	27.4	44.5	44.5	44.5	65	75.2	82.1	44.5	37.6	41	27.4	30.8
Pb	7.3	3.7	10.7	9.1	19.2	11.1	7.9	14.5	22.6	8.6	6.9	20.9	5.4	16.7	16.8
Zn	77	54	78	62	62	86	55	85	40	53	45	82	43	63	64
Ni	27.5	16.4	27	22.2	21.9	27.1	19	28.6	14.9	19.5	16.6	32	14	24.3	23.7
Ti/Zr	33.65	28.83	30.24	29.9	27.64	33.33	28.71	33.6	16.55	32.88	28.27	28.93	24.83	28.28	26.8
Cu/Zn	0.18	0.61	0.11	0.37	0.69	0.17	0.92	0.62	0.34	0.26	0.73	0.03	0.39	0.06	0.05
Cr/Th	3.36	3.46	2.54	2.74	3.62	3.09	4.94	3.96	8.96	9.22	5.49	2.25	5.2	2.15	2.8
Ni/Co	2.35	1.91	1.97	1.9	1.77	1.74	1.96	1.96	1.91	2.41	2.21	2.32	2.03	2.11	2.15
Th/Co	1.48	0.92	0.88	0.85	0.99	0.92	0.93	1.12	1.08	1.1	1.08	1.21	1.14	1.1	1
Th/U	5.09	3.43	5.26	4.35	3.73	4.5	3.75	4.97	3.5	3.18	3	5.06	2.82	4.38	4.23
V/V+Ni	0.81	0.79	0.77	0.79	0.79	0.77	0.77	0.77	0.79	0.78	0.75	0.78	0.78	0.78	0.76
V/Cr	2.05	2.19	2.89	3	1.87	2.09	1.42	1.49	0.73	0.87	1.15	3	1.22	3.11	2.5
Cr/Ni	2.11	1.67	1.14	1.23	2.03	1.64	2.34	2.27	5.05	4.21	2.68	1.18	2.93	1.13	1.3

Table 4. (Continued).

	N20	N22	N23	N24	N26	N28	S1	S2	S3	S4	S5	S6	S8	S9	S11
Ba	130	186	335	202	228	236	321	222	276	350	239	556	223	212	226
Co	6.4	8	6.1	9.3	7.5	9.8	14	9.1	14.1	9.2	11.3	7.2	9.6	12.4	11.6
Cs	3	4.3	2.6	5.8	4.8	5.6	10.7	4.9	7.9	5.2	7.2	3.6	5.3	7.2	7.2
Hf	2.2	2.6	1.8	3.3	3.2	2.5	3.4	2.6	3.3	2.2	3.1	2.8	2.4	3.8	2.8
Nb	5.9	9.3	6.1	8.7	8.8	9.9	11.8	8.9	12	8.1	10.2	6.2	8.5	13.1	11.1
Rb	62.3	82.3	49.6	92.9	80.2	91	149	79.7	126.5	83.7	127.3	57.2	101.6	131.7	120.2
Sr	693.1	359.1	520.7	288.6	409.9	283.8	184.2	502.8	243.9	540.2	372.2	774.4	529.8	219.5	295.5
Th	6.7	12.8	8.6	10.6	10.1	14	17.5	10.4	13.7	10.2	11	7.2	8.6	11.4	12.3
U	2.4	2.8	3.3	2.7	2.7	2.4	3.8	3.1	2.7	3.1	2.6	2.4	2.7	2.5	2.7
V	47	61	47	67	58	79	103	65	81	69	82	52	73	83	77
Zr	68.1	105	76.3	124.3	99.8	98.5	117.9	100.8	116.4	84.5	117.9	93.4	84.3	130.6	106.6

Table 4. (Continued).

Y	15.3	29.4	21.7	21.3	24.6	25.6	26	19.4	28.9	17	22.6	15.5	17.2	21.9	23.2
Cu	67.2	5.9	72.9	1.7	4.1	1.3	7.9	12.2	20.9	17.8	28.4	3.1	32.2	21.2	2.9
Cr	37.6	41	30.8	30.8	27.4	34.2	47.9	34.2	41	34.2	27.4	37.6	41	44.5	41
Pb	6	20.1	11	15.2	16.2	18.2	11.6	6.9	11.7	8.8	12.5	5.4	7.7	12.4	16.9
Zn	40	55	38	59	50	58	82	44	81	53	63	41	54	64	59
Ni	12.9	19.7	11	21	19	23.5	29.2	17.3	28.2	20.3	24.3	14.9	18.2	23	22.1
Ti/Zr	28.19	26.86	25.16	21.24	25.25	29.85	32.57	26.19	28.87	29.11	25.95	22.48	30.6	24.81	28.71
Cu/Zn	1.68	0.11	1.92	0.03	0.08	0.02	0.1	0.28	0.26	0.34	0.45	0.08	0.6	0.33	0.05
Cr/Th	5.62	3.21	3.58	2.9	2.71	2.44	2.74	3.29	3	3.35	2.49	5.23	4.77	3.9	3.34
Ni/Co	2.02	2.46	1.8	2.26	2.53	2.4	2.09	1.9	2	2.21	2.15	2.07	1.9	1.85	1.91
Th/Co	1.05	1.6	1.41	1.14	1.35	1.43	1.25	1.14	0.97	1.11	0.97	1	0.9	0.92	1.06
Th/U	2.79	4.57	2.61	3.93	3.74	5.83	4.61	3.35	5.07	3.29	4.23	3	3.19	4.56	4.56
V/V+Ni	0.78	0.76	0.81	0.76	0.75	0.77	0.78	0.79	0.74	0.77	0.77	0.78	0.8	0.78	0.78
V/Cr	1.25	1.49	1.53	2.18	2.12	2.31	2.15	1.9	1.97	2.02	3	1.38	1.78	1.87	1.88
Cr/Ni	2.92	2.08	2.8	1.47	1.44	1.46	1.64	1.98	1.46	1.68	1.13	2.52	2.25	1.93	1.86

Table 4. (Continued).

	S12	S13	S15	S16	S17	S18	S19	S20	S21	S23	S24	S25	Average	PAAS
Ba	113	297	148	220	263	277	405	334	146	243	164	298	258	650
Co	7.1	15.5	7.8	10.8	5.8	10.9	7.8	6.4	7.9	12.4	6.9	14.5	10.1	23
Cs	2.8	10.3	3.5	7.9	2.3	5.7	3.5	2.6	3.9	7.6	3.1	10.2	6	15
Hf	1.8	3.7	1.9	3	2.7	2.8	2.1	1.8	2	2.8	2.3	3.4	2.7	5
Nb	5.8	12.9	6.8	9.7	5.9	9.2	8.1	6	7.4	9.9	6.7	12.5	9.3	19
Rb	55.3	174.8	71.1	126.8	42.8	110.1	68.4	51.4	76.2	124.2	59.7	163.7	98.6	160
Sr	894.4	201.1	1012.4	353.4	469.2	495.2	492	629.4	655.1	282.2	811.5	199.1	418.1	200
Th	6.1	15.2	6.5	11.7	7.1	11.5	10.9	8	8.4	12.1	7	15	10.9	14.6
U	2.1	2.9	2.3	2.4	2.7	2.8	3.3	2.7	2.3	3.5	2.4	3.6	2.8	3.1
V	35	98	43	71	28	71	43	29	49	73	34	104	69	150
Zr	60.7	127	72.1	100	91.3	94.4	88.2	60.6	79.8	104.6	81.5	125.4	99.6	210
Y	14.1	26.9	14.9	20.5	15.4	21.6	23.6	16.9	17.1	21.4	14	27.1	21.1	27
Cu	8.6	10.8	13	2	71.1	13.4	1.2	32.6	10.9	8.3	8	11.1	19.5	50
Cr	23.9	41	27.4	34.2	23.9	37.6	23.9	20.5	27.4	68.4	27.4	44.5	38.8	110
Pb	4.1	22.6	4.1	18.4	4.5	13.7	13.9	4.5	10.2	18.2	5.5	26	12.1	20
Zn	36	82	41	60	30	53	41	33	41	71	39	79	57	85
Ni	10.4	28	12	22.3	11.5	19.5	14.7	12	15.9	27.7	14.2	31.7	20.5	55
Ti/Zr	26.69	29.29	26.63	30	19.72	28.6	26.53	28.71	26.32	29.83	23.56	29.67	27.71	28.29
Cu/Zn	0.24	0.13	0.32	0.03	2.37	0.25	0.03	0.99	0.27	0.12	0.21	0.14	0.4	0.59
Cr/Th	3.93	2.7	4.21	2.92	3.37	3.27	2.2	2.57	3.26	5.65	3.91	2.96	3.75	7.53
Ni/Co	1.47	1.81	1.54	2.06	1.98	1.79	1.88	1.88	2.01	2.23	2.06	2.19	2.03	2.39
Th/Co	0.86	0.98	0.83	1.08	1.22	1.06	1.4	1.25	1.06	0.98	1.01	1.03	1.09	0.63
Th/U	2.9	5.24	2.83	4.88	2.63	4.11	3.3	2.96	3.65	3.46	2.92	4.17	3.9	4.76
V/V+Ni	0.77	0.78	0.78	0.76	0.71	0.78	0.75	0.71	0.76	0.72	0.71	0.77	0.77	0.73
V/Cr	1.46	2.39	1.57	2.08	1.17	1.89	1.8	1.41	1.79	1.07	1.24	2.34	1.87	1.36
Cr/Ni	2.3	1.47	2.28	1.53	2.08	1.93	1.63	1.71	1.72	2.47	1.93	1.4	2	2

Table 5. Rare earth element concentrations (ppm) of calcareous shale from the Beduh Formation.

	N1	N2	N3	N5	N7	N8	N10	N11	N12	N14	N15	N16	N17	N18	N19	N20
La	41.5	21.3	37	30.3	31.4	39	26.3	44.8	22.8	25.2	23	48.2	22.2	34.3	30.9	19.3
Ce	86.8	41.9	71.1	62.6	67.7	79.5	54.6	91.1	47.7	48.6	46.9	94.1	45.4	70.7	63.4	37.6
Pr	10.75	5.14	8.62	7.56	8.2	9.93	6.67	11.09	5.84	5.94	5.61	10.48	5.38	7.98	7.31	4.31
Nd	38.3	20.5	31.9	28.1	31.1	37.8	25.6	41.8	21.8	20.6	21	34.9	20.8	29.6	26.8	17.4
Sm	6.81	3.85	5.83	5.35	6.44	7.17	5.28	6.6	4.72	3.84	4.31	6.23	3.96	5.06	5.2	3.49
Eu	1.15	0.76	1.09	0.95	1.22	1.22	0.96	1.09	0.91	0.69	0.76	1.02	0.73	0.92	1.02	0.73
Gd	4.45	3.05	4.73	3.67	5.3	4.43	3.59	4.19	4.18	2.69	2.94	5.43	3.12	4.07	4.92	3.47
Tb	0.89	0.48	0.74	0.64	0.91	0.83	0.66	0.93	0.64	0.52	0.54	0.93	0.57	0.81	0.75	0.46
Dy	5.34	2.87	4.37	4.35	4.78	5.3	4.02	5.2	3.44	2.97	3.31	4.85	3.16	3.99	4.13	2.42
Ho	0.92	0.52	0.77	0.76	0.75	0.95	0.72	0.92	0.64	0.57	0.61	0.98	0.56	0.72	0.82	0.5
Er	2.71	1.48	2.06	2.09	1.98	2.78	1.97	2.67	1.81	1.53	1.73	2.74	1.39	2.08	2.15	1.42
Tm	0.38	0.2	0.32	0.29	0.27	0.36	0.25	0.36	0.27	0.2	0.22	0.41	0.2	0.29	0.32	0.19
Yb	2.34	1.33	2.23	1.72	1.69	2.34	1.59	2.29	1.75	1.37	1.3	2.67	1.25	1.7	2.14	1.26
Lu	0.37	0.2	0.38	0.24	0.28	0.38	0.22	0.39	0.31	0.21	0.19	0.44	0.2	0.28	0.33	0.19
ΣREE	202.71	103.58	171.14	148.62	162.02	191.99	132.43	213.43	116.81	114.93	112.42	213.38	108.92	162.5	150.19	92.74
LREE	185.31	93.45	155.54	134.86	146.06	174.62	119.41	196.48	103.77	104.87	101.58	194.93	98.47	148.56	134.63	82.83
HREE	17.4	10.13	15.6	13.76	15.96	17.37	13.02	16.95	13.04	10.06	10.84	18.45	10.45	13.94	15.56	9.91
LREE/HREE	10.65	9.23	9.97	9.8	9.15	10.05	9.17	11.59	7.96	10.42	9.37	10.57	9.42	10.66	8.65	8.36
Ce/Ce*	0.93	0.91	0.9	0.94	0.96	0.92	0.93	0.93	0.94	0.9	0.94	0.95	0.94	0.97	0.96	0.93
Eu/Eu*	0.72	0.77	0.72	0.74	0.72	0.75	0.76	0.72	0.71	0.74	0.74	0.61	0.72	0.7	0.7	0.72
$(La/Yb)_n$	9.98	9.01	9.33	9.91	10.45	9.38	9.3	11	7.33	10.35	9.95	10.15	9.99	11.35	8.12	8.62
$(Nd/Yb)_n$	5.17	4.87	4.52	5.16	5.81	5.1	5.08	5.76	3.93	4.75	5.1	4.13	5.26	5.5	3.96	4.36
$(Dy/Yb)_n$	1.37	1.3	1.18	1.52	1.7	1.36	1.52	1.37	1.18	1.3	1.53	1.09	1.52	1.41	1.16	1.15
$(La/Sm)_n$	3.84	3.48	3.99	3.56	3.07	3.42	3.14	4.27	3.04	4.13	3.36	4.87	3.53	4.27	3.74	3.48

Table 5. (Continued).

	N22	N23	N24	N26	N28	S1	S2	S3	S4	S5	S6	S8	S9	S11	S12
La	35.9	25.1	30	29.5	36.9	44.2	26.7	40.8	26.4	29.8	21.3	24.4	31.9	33.1	18.6
Ce	69.5	51.8	56.1	61.5	78.3	87.2	53.9	81.9	52.4	60.4	43.6	47.7	62.1	66.4	36.9
Pr	8.16	6.2	6.39	6.9	9.45	10.09	6.09	8.66	6.11	6.85	4.64	5.2	7.53	8.15	4.52
Nd	31	24.7	23.9	26.4	35.9	36.4	21.1	31.6	21.8	25.7	15.6	18.5	29.5	31.9	17.1
Sm	6.12	5.31	4.24	5.2	6.69	6.07	4.05	5.44	4.26	5.06	3.14	3.57	5.85	6.56	3.64
Eu	1.3	1.1	0.79	1.03	1.21	1.06	0.73	1.13	0.76	0.99	0.59	0.73	1.14	1.26	0.7
Gd	6.37	4.64	4.46	4.88	4.69	4.78	3.17	5.77	3.22	4.29	3.34	3.58	5.04	4.83	2.96
Tb	0.88	0.75	0.67	0.71	0.93	0.88	0.66	0.89	0.62	0.65	0.51	0.52	0.68	0.74	0.43
Dy	4.67	4.08	3.35	3.56	4.98	4.73	3.51	4.4	2.93	3.49	2.42	2.39	4.25	4.65	2.62
Ho	0.9	0.77	0.66	0.73	0.97	0.98	0.72	0.87	0.6	0.74	0.48	0.52	0.87	0.89	0.53
Er	2.43	1.99	1.77	2.01	2.57	2.67	1.83	2.52	1.64	2.09	1.19	1.54	2.31	2.5	1.47
Tm	0.37	0.29	0.26	0.3	0.37	0.4	0.26	0.36	0.24	0.33	0.18	0.22	0.39	0.36	0.19
Yb	2.41	1.79	1.79	2.05	2.22	2.47	1.57	2.5	1.66	2.12	1.18	1.62	2.48	2.33	1.38
Lu	0.39	0.28	0.29	0.33	0.34	0.37	0.25	0.41	0.23	0.33	0.19	0.25	0.35	0.35	0.18

Table 5. (Continued).

ΣREE	170.4	128.8	134.67	145.1	185.52	202.3	124.54	187.25	122.87	142.84	98.36	110.74	154.39	164.02	91.22
LREE	151.98	114.21	121.42	130.53	168.45	185.02	112.57	169.53	111.73	128.8	88.87	100.1	138.02	147.37	81.46
HREE	18.42	14.59	13.25	14.57	17.07	17.28	11.97	17.72	11.14	14.04	9.49	10.64	16.37	16.65	9.76
LREE/HREE	8.25	7.83	9.16	8.96	9.87	10.71	9.4	9.57	10.03	9.17	9.36	9.41	8.43	8.85	8.35
Ce/Ce*	0.92	0.94	0.92	0.98	0.95	0.94	0.96	0.99	0.94	0.96	0.99	0.96	0.91	0.92	0.91
Eu/Eu*	0.72	0.76	0.63	0.71	0.75	0.68	0.7	0.7	0.71	0.73	0.63	0.7	0.72	0.77	0.74
$(La/Yb)_n$	8.38	7.89	9.43	8.1	9.35	10.07	9.57	9.18	8.95	7.91	10.15	8.47	7.24	7.99	7.58
$(Nd/Yb)_n$	4.06	4.36	4.22	4.07	5.11	4.65	4.24	3.99	4.15	3.83	4.18	3.61	3.76	4.32	3.91
$(Dy/Yb)_n$	1.16	1.37	1.12	1.04	1.35	1.15	1.34	1.06	1.06	0.99	1.23	0.89	1.03	1.2	1.14
$(La/Sm)_n$	3.69	2.98	4.45	3.57	3.47	4.58	4.15	4.72	3.9	3.71	4.27	4.3	3.43	3.18	3.22

Table 5. (Continued).

	S13	S15	S16	S17	S18	S19	S20	S21	S23	S24	S25	average	PAAS
La	41.3	20	33.4	20.7	32.8	32.9	24.1	25.6	36.5	19.5	43.7	30.54	38.2
Ce	80.2	38.5	65.8	41.4	63.8	67.1	48.5	48.7	73	36.9	86.1	61.18	79.6
Pr	9.62	4.86	8.03	5.28	7.59	7.89	6.09	6.05	8.74	4.36	10.23	7.25	8.83
Nd	35.6	19.6	30.4	20.6	27.8	31.7	24	23.5	31.9	17.3	39.7	27.17	33.9
Sm	6.32	3.95	5.65	4.39	5.64	6.33	5.01	5.01	5.98	3.36	7.14	5.19	5.55
Eu	1.26	0.79	1.05	0.88	1.16	1.14	0.94	0.9	1.07	0.67	1.3	0.97	1.08
Gd	5.44	3.39	4	3.66	4.43	5.14	3.6	3.49	4.24	3.05	5.38	4.19	4.66
Tb	0.79	0.44	0.64	0.54	0.66	0.75	0.54	0.55	0.69	0.41	0.88	0.68	0.77
Dy	4.9	2.75	4.32	3.08	4.09	5.07	3.51	3.45	4.35	2.7	5.44	3.91	4.68
Ho	0.94	0.49	0.78	0.56	0.74	0.89	0.59	0.63	0.76	0.46	0.99	0.73	0.99
Er	2.93	1.46	2.28	1.67	2.13	2.51	1.8	1.82	2.21	1.35	2.96	2.05	2.85
Tm	0.41	0.24	0.32	0.21	0.33	0.37	0.26	0.25	0.35	0.2	0.44	0.3	0.41
Yb	2.97	1.49	1.97	1.45	2.12	2.43	1.57	1.72	2.21	1.4	2.78	1.92	2.82
Lu	0.42	0.21	0.32	0.22	0.32	0.32	0.24	0.27	0.37	0.21	0.44	0.3	0.43
ΣREE	193.1	98.17	158.96	104.64	153.61	164.54	120.75	121.94	172.37	91.87	207.48	146.4	184.77
LREE	174.3	87.7	144.33	93.25	138.79	147.06	108.64	109.76	157.19	82.09	188.17	132.3	167.16
HREE	18.8	10.47	14.63	11.39	14.82	17.48	12.11	12.18	15.18	9.78	19.31	14.08	17.61
LREE/HREE	9.27	8.38	9.87	8.19	9.37	8.41	8.97	9.01	10.36	8.39	9.74	9.40	9.49
Ce/Ce*	0.91	0.89	0.91	0.9	0.92	0.94	0.91	0.89	0.93	0.91	0.92	0.93	
Eu/Eu*	0.74	0.74	0.76	0.76	0.8	0.69	0.76	0.74	0.73	0.72	0.72	0.72	
$(La/Yb)_n$	7.82	7.55	9.54	8.03	8.7	7.62	8.64	8.37	9.29	7.84	8.84	8.97	
$(Nd/Yb)_n$	3.79	4.15	4.87	4.49	4.14	4.12	4.83	4.32	4.56	3.9	4.51	4.49	
$(Dy/Yb)_n$	1	1.11	1.32	1.27	1.16	1.25	1.34	1.21	1.18	1.16	1.17	1.24	
$(La/Sm)_n$	4.11	3.19	3.72	2.97	3.66	3.27	3.03	3.22	3.84	3.65	3.85	3.7	

5.3. Provenance

The chemical composition of siliciclastic sedimentary rocks can be related to their source region chemical composition (e.g., Madhavaraju and Lee, 2010; Nagarajan et al., 2011; Moosavirad et al., 2011; Hofer et al., 2013; Armstrong-Altrin, 2014; Armstrong-Altrin et al., 2015 a, 2015b). In order to infer the provenance of siliciclastic rocks, several major, trace, and rare earth element-based discrimination diagrams have been proposed by various authors (e.g., Roser and Korsch, 1988; Floyd et al. 1989, 1990; McLennan

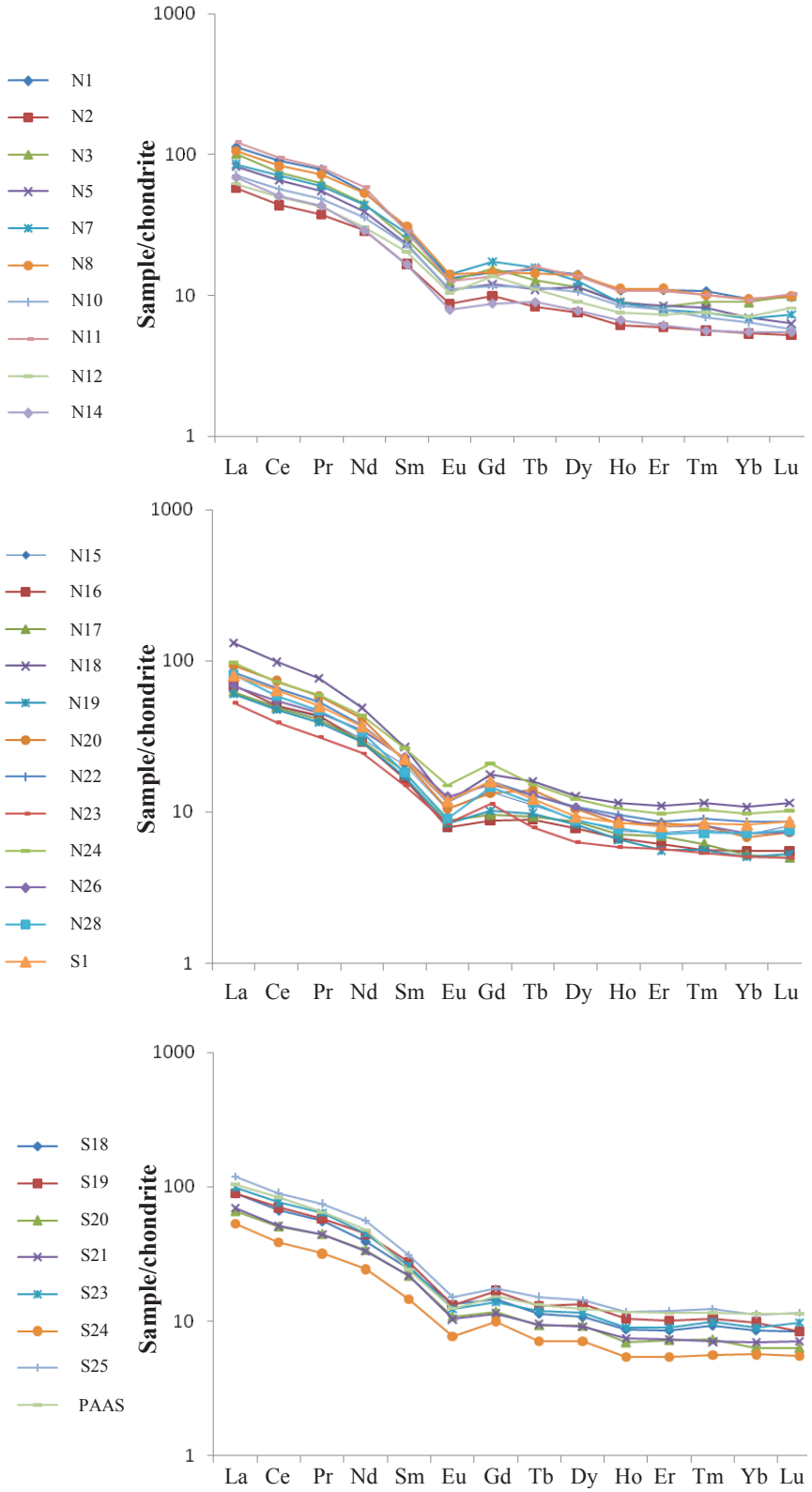

Figure 7. Chondrite normalized rare earth elements plot for shale samples from the Beduh Formation; chondrite normalization values are from Taylor and McLennan (1985).

Table 6. Correlation matrix for the clay minerals and major oxides for the calcareous shale of the Beduh Formation.

	Illite	Kaolinite	Smectite	Chlorite	Illite chemistry index	Illite crystallinity index	Kaolinite crystallinity index	SiO_2	Al_2O_3	Fe_2O_3	CaO	MgO	Na_2O	K_2O	MnO	TiO_2	P_2O_5
Illite	1																
Kaolinite	–0.733	1															
Smectite	–0.011	–0.671	1														
Chlorite	–0.517	0.586	–0.567	1													
Illite chemistry index	–0.230	0.161	–0.166	0.490	1												
Illite crystallinity index	–0.694	**0.919**	–0.677	0.067	–0.037	1											
Kaolinite crystallinity index	**0.738**	**–0.974**	0.643	–0.626	–0.221	**–0.924**	1										
SiO_2	0.650	–0.587	0.205	–0.357	0.175	–0.492	0.459	1									
Al_2O_3	0.659	–0.597	0.193	–0.248	0.150	–0.510	0.465	**0.987**	1								
Fe_2O_3	0.585	–0.527	0.214	–0.250	0.113	–0.440	0.398	**0.976**	**0.983**	1							
CaO	–0.641	0.579	–0.203	0.316	–0.154	0.483	–0.447	**–0.997**	**–0.995**	**–0.986**	1						
MgO	0.325	–0.213	0.074	–0.149	0.068	–0.095	0.048	**0.845**	**0.864**	**0.914**	**–0.870**	1					
Na_2O	–0.289	0.325	0.050	–0.609	–0.280	0.506	–0.364	–0.001	–0.108	0.001	0.020	0.194	1				
K_2O	0.662	–0.605	0.183	–0.228	0.175	–0.524	0.477	**0.983**	**0.998**	**0.979**	**–0.991**	**0.850**	–0.146	1			
MnO	**–0.888**	0.615	0.094	0.117	0.088	0.564	–0.552	**–0.775**	**–0.811**	**–0.741**	**0.783**	–0.590	0.289	**–0.808**	1		
TiO_2	0.719	–0.642	0.193	–0.298	0.190	–0.583	0.529	**0.987**	**0.974**	**0.947**	**–0.981**	**0.779**	–0.069	**0.971**	**–0.827**	1	
P_2O_5	0.633	–0.538	0.115	–0.419	0.341	–0.569	0.508	0.719	0.628	0.597	–0.673	0.348	0.078	0.630	–0.564	**0.777**	1

Underlined: Significant at 0.05 level.
Bolded: Significant at 0.01 level.
No. of samples = 42.

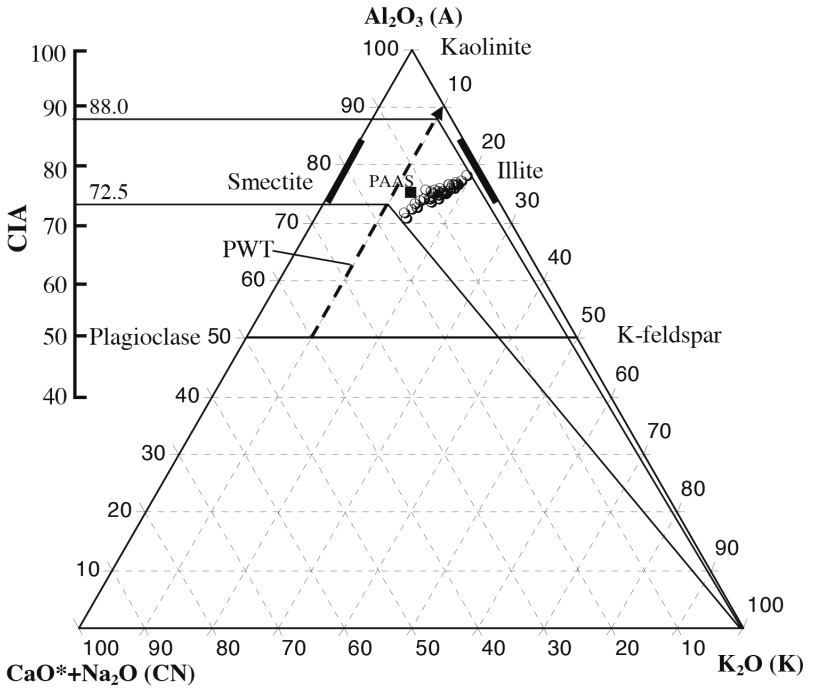

Figure 8. A-CN-K ternary plot for the shale samples from Beduh Formation (Nesbitt and Young, 1984; Fedo et al., 1995); dashed-line arrow represents the predicted weather trend (PWT) for the shale samples.

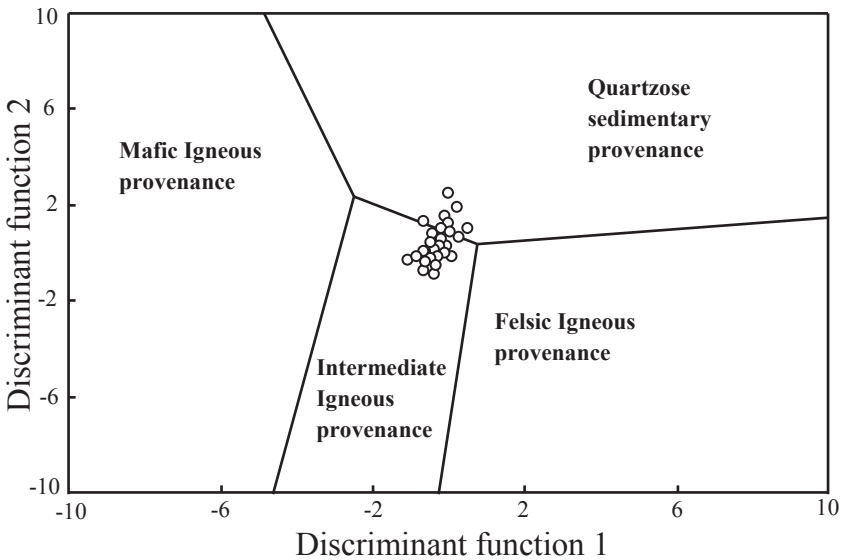

Figure 9. Provenance discrimination function diagram for the Beduh shales (after Roser and Korsch, 1988). Discriminant function 1 = $30.6038TiO_2/Al_2O_3 - 12.541Fe_2O_3/Al_2O_3 + 7.329MgO/Al_2O_3 + 12.031Na_2O/Al_2O_3 + 35.42K_2O/Al_2O_3 - 6.382$. Discriminant function 2 = $56.500TiO_2/Al_2O_3 - 10.879Fe_2O_3/Al_2O_3 + 30.875MgO/Al_2O_3 - 5.404Na_2O/Al_2O_3 + 11.112K_2O/Al_2O_3 - 3.89$.

et al., 1993; Mortazavi et al., 2014). In the provenance discrimination diagram of Roser and Korsch (1988), the discriminant functions are based on concentrations of both immobile and mobile major elements. On this plot the Beduh shales fall in the fields of quartzose sedimentary and intermediate igneous provenances (Figure 9). In the

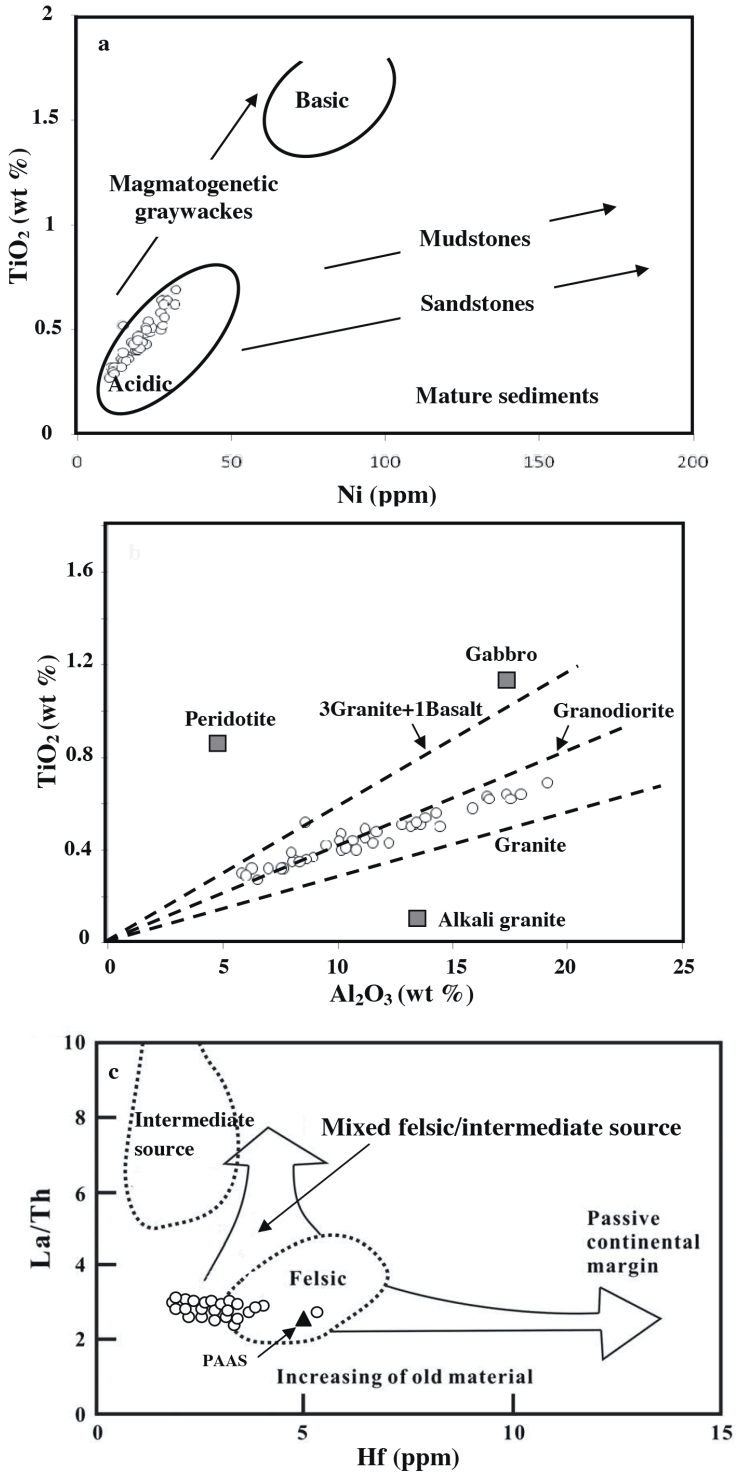

Figure 10. Provenance discrimination diagrams: a) TiO_2 versus Ni bivariate diagram (after Floyd et al., 1989), b) TiO_2 versus Al_2O_3 bivariate diagram (after McLennan et al., 1979) where the "granite line" and "3 granite + 1 basalt line" are after Schieber (1992), c) La/Th versus Hf bivariate diagram (after Floyd and Leveridge, 1987).

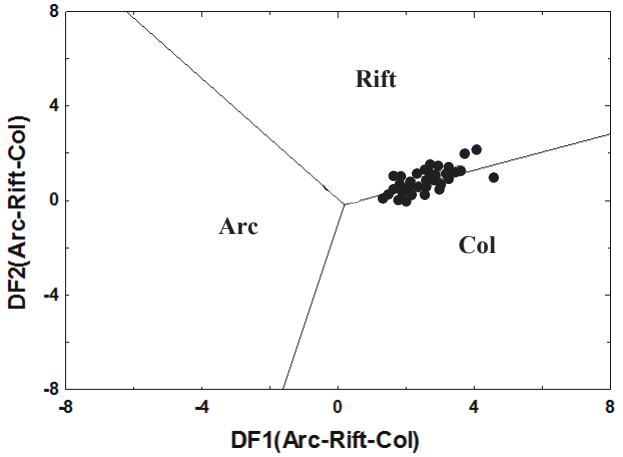

Figure 11. Discriminant function diagrams for low-silica clastic sediments for studied shale samples of the Beduh Formation (after Verma and Armstrong-Altrin, 2013). Discriminant function equations are: DF1(Arc-Rift-Col)m2 = (0.608 × $\ln(TiO_2/SiO_2)_{adj}$) + (−1.854 × $\ln(Al_2O_3/SiO_2)_{adj}$) + (0.299 × $\ln(Fe_2O_3^t/SiO_2)_{adj}$) + (−0.550 × $\ln(MnO/SiO_2)_{adj}$) + (0.120 × $\ln(MgO/SiO_2)_{adj}$) + (0.194 × $\ln(CaO/SiO_2)_{adj}$) + (−1.510 × $\ln(Na_2O/SiO_2)_{adj}$) + (1.941 × $\ln(K_2O/SiO_2)_{adj}$) + (0.003 × $\ln(P_2O_5/SiO_2)_{adj}$) − 0.294. DF2(Arc-Rift-Col)m2 = (−0.554 × $\ln(TiO_2/SiO_2)_{adj}$) + (−0.995 × $\ln(Al_2O_3/SiO_2)_{adj}$) + (1.765 × $\ln(Fe_2O_3t/SiO_2)_{adj}$) + (−1.391 × $\ln(MnO/SiO_2)_{adj}$) + (−1.034 × $\ln(MgO/SiO_2)_{adj}$) + (0.225 × $\ln(CaO/SiO_2)_{adj}$) + (0.713 × $\ln(Na_2O/SiO_2)_{adj}$) + (0.330 × $\ln(K_2O/SiO_2)_{adj}$) + (0.637 × $\ln(P_2O_5/SiO_2)_{adj}$) − 3.631.

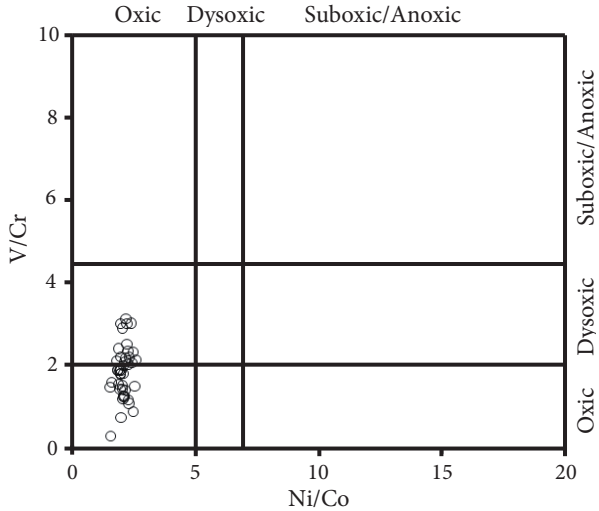

Figure 12. Cross plots of trace elements ratios (V/Cr vs. Ni/Co) used as paleoredox proxies (after Jones and Manning, 1994).

TiO_2-Ni bivariate diagram (Floyd et al., 1989), the studied shales plot in the acidic rocks field (Figure 10a). These results (i.e. acidic and intermediate) can be confirmed with other diagrams such as TiO_2 versus Al_2O_3 (McLennan et al., 1980) and the La/Th versus Hf bivariate diagrams (Floyd and Leveridge, 1987). On these plots the studied shales fall mostly in the field of felsic rocks (Figures 10b and 10c). The Al_2O_3/TiO_2 ratio in clastic rocks is used to determine the composition of the source rocks, because this ratio increases from 3 to 8 for mafic rocks, 8 to 21 for intermediate rocks, and 21 to 70 for felsic igneous rocks (Hayashi et al., 1997). The average value of the Al_2O_3/TiO_2 ratio for the studied shale is 24.53 (Table 2). The average K_2O/Na_2O ratio (Table 2) favors a significant contribution of felsic components rather than mafic in the source area.

Unlike alkaline earth elements, HFSEs (including Zr, Ti, Y, Nb, Th, and Hf) and some TTEs (e.g., Cr, Ni, and Co) as well as REEs are the most suitable provenance indicators, because of their relatively low mobility during sedimentary processes (e.g., McLennan et al., 1990). Elevated Cr and Ni abundances (Cr > 150 ppm, Ni > 100 ppm) are indicative of mafic or ultramafic provenance (Wrafter and Graham, 1989; Garver et al., 1996; Armstrong-Altrin et al., 2004). In comparison with PAAS, the relatively low abundances of Cr, Ni, and Co in the studied shale (Table 4) suggest no significant occurrence of mafic or ultramafic rocks in the source area.

Cullers (1994) proposed that sediments with Cr/Th ratios ranging from 2.5 to 17.5 and Eu/Eu* values from 0.48 to 0.78 are indicative of felsic sources. The values of the Cr/Th and Eu/Eu* in the studied samples (3.75 and 0.70, respectively) generally fall within the felsic range. Th/Co values commonly trace the existence of felsic and/or mafic components within these values (Cullers, 1994, 2000; Armstrong-Altrin et al., 2004). In the Beduh Shale, the Th/Co is ideal for felsic rocks (Table 4).

Additionally, the REE patterns can also be used to infer the source of sediments since felsic rocks contain high LREE/HREE ratios and negative Eu anomalies, whereas mafic rocks usually contain low LREE/HREE ratios and no Eu anomalies (e.g., Cullers and Graf, 1983; Absar et al., 2009; Absar and Sreenivas, 2015). The LREE-enriched and flat HREE pattern of the studied shale is similar to the PAAS (Figure 7) and Precambrian Shield of the Arabian-Nubian Plate (Gebreyohannes, 2014), which indicates a felsic source. Accordingly, the felsic and intermediate igneous rocks are suggested as source rocks for the shales of the Beduh Formation.

5.4. Tectonic setting

Various discrimination diagrams, based on major element compositions of clastic sediments, are widely used to identify the tectonic setting of unknown basins (Bhatia, 1983; Roser and Korsch, 1986), although numerous studies identified that the results inferred from these discrimination diagrams were inconsistent with the geology of the studied areas (Valloni and Maynard, 1981; Dostal and Keppie, 2009). The use of these conventional discrimination diagrams has been cautioned against by

many researchers (e.g., Armstrong-Altrin and Verma, 2005; Ryan and Williams, 2007; Armstrong-Altrin, 2015; Verma and Armstrong-Altrin, 2016).

Recently, Verma and Armstrong-Altrin (2013) proposed two discriminant function-based major element diagrams for the tectonic discrimination of siliciclastic sediments from 3 main tectonic settings: island or continental arc, continental rift, and collision, created for the tectonic discrimination of high-silica [$(SiO_2)_{adj}$ = 63%–95%] and low-silica [$(SiO_2)_{adj}$ = 35%–63%] types. In addition, Armstrong-Altrin (2015) evaluated these two tectonic discrimination diagrams and recommended that the two multidimensional diagrams can be considered as a tool for successfully discriminating the tectonic setting of older sedimentary basins. These discrimination diagrams were successfully used in recent studies to discriminate the tectonic setting of a source region based on the geochemistry of clastic sediments (Nagarajan et al., 2015; Tawfik et al., 2015; Zaid et al., 2015).

These discriminant function-based major element diagrams were used in this study to identify the tectonic environment of the Beduh shales. On the low-silica multidimensional diagram (Figure 11), the Beduh shales were plotted in the rift and collision fields, which is consistent with the geology of the Arabian Shield and the Rutba Uplift (Jassim and Goff, 2006) and reveals the possibility that the Beduh shales may consist of sediments derived from active regions of the Mid-Oceanic Ridge (Figure 3). In addition it is suggested that the shales of the Beduh Formation also received sediments by volcanic activity, indicated by the presence of volcaniclastic materials (glass shards and glassy spherules) and smectite as a mixed layer with illite (Hakeem, 2012).

5.5. Paleoredox conditions

Previous studies showed that redox sensitive elements, such as Cu, Zn, V, Ni, Cr, and U, in the sediments can be used as a powerful tool for evaluation of the paleoredox conditions (Jones and Manning, 1994; Madhavaraju and Ramasamy, 1999; McKirdy et al., 2011; Armstrong-Altrin et al., 2015a; Hu et al., 2015).

The U/Th ratio may be used as a redox indicator, being higher in organic-rich mudstones (Jones and Manning, 1994). U/Th ratios below 1.25 suggest oxic conditions of deposition, whereas elevated values indicate suboxic and anoxic conditions (Jones and Manning, 1994; Nath et al., 1997; Akinyemi et al., 2013). The present study shows a lower U/Th ratio (0.17–0.38, avg. = 0.27) for these shales (Table 4), indicating deposition in an oxic environment.

Jones and Manning (1994) and Rimmer (2004) used the elemental ratios (Ni/Co and V/Cr) to deduce the redox conditions during the deposition of the shale. The higher Ni/Co and V/Cr ratios are related to low oxygen levels during the deposition. Jones and Manning (1994) and Sari and Koca (2012) suggested that Ni/Co ratios below 5 indicate oxic environments, whereas ratios of 5–7 indicate dysoxic environments and ratios above 7 suboxic to anoxic. The studied shale shows a lower Ni/Co ratio (1.47– 2.53; avg. = 2.03; Table 4). This ratio suggests an oxic depositional environment during deposition of sediments (Figure 12). Jones and Manning (1994) and Armstrong-Altrin et al. (2015a) used the V/Cr ratio to infer the depositional environment. A V/Cr ratio below 2 refers to oxic, 2.0–4.25 to dysoxic, and higher than 4.25 to suboxic to anoxic conditions. V/Cr ratios of the studied shale samples vary from 0.73 to 3.11 with an average ratio value of 1.87 (Table 4), indicating an oxic condition (Figure 12).

Hallberg (1976) stated that the Cu/Zn ratio in the sediment may reflect redox conditions during deposition and the ratio increases in reduced conditions and decreases in oxidizing conditions. The lower Cu/Zn ratio (0.02–2.37, avg. = 0.40; Table 4) in the studied shale reinforces deposition under oxidizing conditions.

6. Conclusions

The clay minerals of the shale comprise illite, kaolinite, and chlorite, with a minor mixed layer of illite/smectite and illite/chlorite. Calcite and quartz are the main nonclay species with subordinate amounts of feldspar and hematite. The shale of the Beduh Formation shows high CaO content (due to the high carbonate content), which is due to the dilution effect compared to other oxides and trace and rare earth elements. The mineralogical and geochemical parameters like illite crystallinity, CIA and CIW values, and Th/U ratios reveal moderate to intense chemical weathering in the source area. Major, trace, and rare earth elements imply that the shale was derived from dominantly felsic and intermediate (granite and granitoid) source rocks, probably from the plutonic-metamorphic complex of the Arabian Shield and Rutba Uplift to the southwest of the basin. The U/Th, V/Cr, Ni/Co, and Cu/Zn ratios and negative Eu anomaly suggest deposition under an oxic environment. The tectonic setting discrimination diagram reveals active and passive tectonic environments for the source area; the sediments were probably derived from the Arabian Shield and Rutba Uplift.

Acknowledgments

This research is part of the MSc thesis work submitted by Sirwa S Shangola at Salahaddin University. We are grateful to Dr Hikmat S Mustafa and Dr Farhad A Hakeem, Salahaddin University, for their help during field work.

References

Absar N, Raza M, Roy M, Naqvi SM, Roy AK (2009). Composition and weathering conditions of Paleoproterozoic upper crust of Bundelkhand craton, Central India: records from geochemistry of clastic sediments of 1.9 Ga Gwalior Group. Precamb Res 168: 313-329.

Absar N, Sreenivas B (2015). Petrology and geochemistry of greywackes of the ~1.6 Ga Middle Aravalli Supergroup, northwest India: evidence for active margin processes. Int Geol Rev 57: 134-158.

Akinyemi SA, Adebayo OF, Ojo OA, Fadipe OA, Gitari WM (2013). Mineralogy and geochemical appraisal of Paleo-redox indicators in Maastrichtian outcrop shales of Mamu Formation, Anambra Basin, Nigeria. J Natur Sci Res 3: 48-64.

Al-Brifkani MJN (2008). Structural and tectonic analysis of the Northern Thrust Zone (East Khabour River) in Iraq. PhD, University of Mosul, Mosul, Iraq (in Arabic).

Armstrong-Altrin JS (2015). Evaluation of two multidimensional discrimination diagrams from beach and deep-sea sediments from the Gulf of Mexico and their application to Precambrian clastic sedimentary rocks. Int Geol Rev 57: 1446-1461.

Armstrong-Altrin JS, Lee YI, Verma SP, Ramasamy S (2004). Geochemistry of sandstones from the upper Miocene Kudankulam Formation, southern India: implications for provenance, weathering, and tectonic setting. J Sed Res 74: 285-297.

Armstrong-Altrin JS, Machain-Castillo ML, Rosales-Hoz L, Carranza-Edwards A, Sanchez-Cabeza J, Ruíz-Fernández AC (2015a). Provenance and depositional history of continental slope sediments in the Southwestern Gulf of Mexico unraveled by geochemical analysis. Continental Shelf Res 95: 15-26.

Armstrong-Altrin JS, Nagarajan R, Balaram V, Natalhy-Pineda O (2015b). Petrography and geochemistry of sands from the Chachalacas and Veracruz beach areas, western Gulf of Mexico, Mexico: constraints on provenance and tectonic setting. J South Amer Earth Sci 64: 199-216.

Armstrong-Altrin JS, Verma SP (2005). Critical evaluation of six tectonic setting discrimination diagrams using geochemical data of Neogene sediments from known tectonic setting. Sediment Geol 177: 115-129.

Bellen RC, Dunnington HV, Wetzel R, Morton D (1959). Lexique Stratigraphique Internal Asie. Iraq. International Geological Congress. Fasc. 10a. Paris, France: Commission on Stratigraphy (in French).

Bhat MI, Ghosh SK (2001). Geochemistry of the 2.51 Ga old Rampur group pelites, western Himalayas: implications for their provenance and weathering. Precamb Res 108: 1-16.

Bhatia MR (1983). Plate tectonics and geochemical composition of sandstones. J Geol 91: 611-627.

Bhatia MR, Crook KAW (1986). Trace element characteristics of greywackes and tectonic setting discrimination of sedimentary basins. Contrib Mineral Petrol 92: 181-193.

Buday T (1980). The Regional Geology of Iraq, Stratigraphy and Paleontology. Mosul, Iraq: Dar Al-Kutb Publishing House.

Carroll D (1970). Clay Minerals: A Guide to their X-Ray Identification. Boulder, CO, USA: Geological Society of America.

Condie KC (1991). Another look at rare earth elements in shales. Geochim Cosmochim Ac 55: 2527-2531.

Cullers RL (1994). The controls on major and trace element variation of shales, siltstones, and sandstones of Pennsylvanian-Permian age from uplifted continental blocks in Colorado to platform sediment in Kansas, USA. Geochim Cosmochim Ac 58: 4955-4972.

Cullers RL (2000). The geochemistry of shales, siltstones, and sandstones of Pennsylvanian-Permian age, Colorado, USA: implication for provenance and metamorphic studies. Lithos 51: 181-203.

Cullers RL, Graf J (1983). Rare earth elements in igneous rocks of the continental crust: intermediate and silicic rocks, ore petrogenesis. In: Henderson P, editor. Rare-Earth Geochemistry. Amsterdam, the Netherlands: Elsevier, pp. 275-312.

Dostal J, Keppie JD (2009). Geochemistry of low-grade clastic rocks in the Acatlán Complex of southern Mexico: evidence for local provenance in felsic-intermediate igneous rocks. Sediment Geol 222: 241-253.

Dunoyer de Segonzac D (1969). Les mineraux argileux dans la diagenese passage au metamorphisme. Memoires du Service de la Carte Geologique de Lorraine 29. Paris, France: Centre National de la Recherche Scientifique (in French).

Etemad-Saeed N, Hosseini-Barzi M, Armstrong-Altrin JS (2011). Petrography and geochemistry of clastic sedimentary rocks as evidences for provenance of the Lower Cambrian Lalun Formation, Posht-e-badam block, Central Iran. J Afr Earth Sci 61: 142-159.

Fedo CM, Eriksson K, Krogstad EJ (1996). Geochemistry of shale from the Archean (~3.0 Ga) Buhwa Greenstone belt, Zimbabwe: implications for provenance and source area weathering. Geochim Cosmochim Ac 60: 1751-1763.

Fedo CM, Nesbitt HW, Young GM (1995). Unraveling the effects of potassium metasomatism in sedimentary rocks and paleosols, with implications for paleoweathering conditions and provenance. Geology 23: 921-924.

Feng R, Kerrich R (1990). Geochemistry of fine grained clastic sediments in the Archean Abitib greenstones belt, Canada: implications for provenance and tectonic setting. Geochim Cosmochim Ac 54: 1061-1081.

Floyd PA, Franke W, Shail R, Dorr W (1990). Provenance and depositional environment of Rhenohercynian synorgenic greywacke from the Giessen nappe, Germany. Geologische Rundschau 79: 611-626.

Floyd PA, Leveridge BE (1987). Tectonic environment of the Devonian Gramscatho basin, south Cornwall: framework mode and geochemical evidence from turbiditic sandstones. J Geol Soci London 144: 531-542.

Floyd PA, Winchester JA, Park RG (1989). Geochemistry and tectonic setting discrimination using immobile elements. Earth Planet Sci Lett 27: 211-218.

Friedman G, Johnson KG (1982). Exercises in Sedimentology. New York, NY, USA: John Wiley and Sons.

Garver JI, Royce PR, Smick TA (1996). Chromium and nickel in shale of the Taconic Foreland: a case study for the provenance of fine-grained sediments with an ultramafic source. J Sediment Res 66: 100-106.

Gebreyohannes GW (2014). Geology, geochemistry and geochronology of Neoproterozoic rocks in western Shire, Northern Ethiopia. MSc, University of Oslo, Oslo, Norway.

Girty GH, Ridge DL, Knaack C, Johnson D, Riyami RK (1996). Provenance and depositional setting of Paleozoic chert and argillite, Sierra Nevada, California. J Sediment Res 66:107-118.

Grim RE (1968). Clay Mineralogy. 2nd ed. New York, NY, USA: McGraw-Hill.

Hakeem FA (2012). Sedimentology and suitability for some ceramic industries of Beduh Formation (Lower Triassic), Norther Thrust Zone, Kurdistan Region. PhD, Salahaddin University, Erbil, Iraq.

Hallberg RO (1976). A geochemical method for investigation of paleoredox conditions in sediments. Ambio Special Report 4: 139-147.

Harnois L (1988). The CIW index: a new chemical index of weathering. Sediment Geol 55: 319-322.

Hayashi K, Fujisawa H, Holland HD, Ohmoto H (1997). Geochemistry of ~1.9 Ga sedimentary rocks from northeastern Labrador, Canada. Geochim Cosmochim Ac 61: 4115-4137.

Hemming SR, McLennan SM, Hanson GN (1995). Geochemical and Nd/Pb isotopic evidence for the provenance of the Early Proterozoic Virginia Formation, Minnesota: implication for the tectonic setting of the Animikie basin. J Geol 103: 147-168.

Hofer G, Wagreich M, Neuhuber S (2013). Geochemistry of fine grained sediments of the Upper Cretaceous to Paleogene Gosau Group (Austria, Slovakia): implications for paleoenvironmental and provenance studies. Geosci Front 4: 449-468.

Hu J, Li Q, Li J, Huang J, Ge D (2015). Geochemical characteristics and depositional environment of the Middle Permian mudstones from central Qiangtang Basin, northern Tibet. Geol J (in press).

Jahn BM, Condie KC (1995). Evolution of the Kaapvaal Craton as viewed from geochemical and Sm-Nd isotopic analyses of intracratonic pelites. Geochim Cosmochim Ac 59: 2239-2258.

Jassim SZ, Buday T, Cicha I (2006). Tectonic framework. In: Jassim SZ, Goff JC, editors. Geology of Iraq. Prague, Czech Republic: Dolin, pp. 45-56.

Jassim SZ, Goff JC (2006). Phanerozoic development of the Northern Arabian Plate. In: Jassim SZ, Goff JC, editors. Geology of Iraq. Prague, Czech Republic: Dolin, pp. 15-34.

Jones B, Manning DAC (1994). Comparison of geochemical indices used for the interpretation of paleoredox conditions in ancient mudstones. Chem Geol 111: 111-129.

Kübler B (1967). La cristallinité de l'illite et les zones tout à fait supérieures du métamorphisme. In: Etage Techniques, Colloque de Neuchatel. Neuchâtel, Switzerland: Baconniere, pp. 105-121 (in French).

Madhavaraju J, Ramasamy S (1999). Rare earth elements in limestones of Kallankurich-chi Formation of Ariyalur Group, Tiruchirapalli Cretaceous, Tamil Nadu. J Geol Soc India 54: 291-301.

McKirdy DM, Hall PA, Nedin C, Halverson GP, Michaelsen BH, Jago JB, Gehling JG, Jenkins RJF (2011). Paleoredox status and thermal alteration of the lower Cambrian (Series 2) Emu Bay Shale Lagerstätte, South Australia. Australian J Earth Sci 58: 259-272.

McLennan SM (1989). Rare earth elements in sedimentary rocks: Influence of provenance and sedimentary processes. In: Lipin BR, McKay GA, editors. Geochemistry and Mineralogy of Rare Earth Elements. Rev Mineral 21: 169-200.

McLennan SM, Fryer BJ, Young GM (1979). The geochemistry of the carbonate rich Espanola Formation (Huronian) with emphasis on the rare earth elements. Can J Earth Sci 16: 230-239.

McLennan S, Hemming S, McDaniel D, Hanson G (1993). Geochemical approaches to sedimentation, provenance, and tectonics. Geol Soc Am Spec Pap 284: 21-40.

McLennan SM, Taylor SR (1991). Sedimentary rocks and crustal evolution: tectonic setting and secular trends. J Geol 99: 1-21.

McLennan SM, Taylor SR, Mcculloch MT, Maynard JB (1990). Geochemical and Nd-Sr isotopic composition of deep-sea turbidites: crustal evolution and plate tectonic associations. Geochim Cosmochim Ac 54: 2015-2050.

Millot G (1964). Geologie des Argiles. Paris, France: Masson et Compagnie (in French).

Moosavirad SM, Janardhana MR, Sethumadhav MS, Moghadam MR, Shankara M (2011). Geochemistry of lower Jurassic shales of the Shemshak Formation, Kerman Province, Central Iran: provenance, source weathering and tectonic setting. Chemie der Erde 71: 279-288.

Mortazavi M, Moussavi-Harami R, Mahboubi A, Nadjafi M (2014). Geochemistry of the Late Jurassic–Early Cretaceous shales (Shurijeh Formation) in the intracontinental Kopet-Dagh Basin, northeastern Iran: implication for provenance, source weathering, and paleoenvironments. Arab J Geosci 7: 5353-5366.

Nagarajan R, Armstrong-Altrin JS, Kessler FL, Hidalgo-Moral El, Dodge-Wan D, Taib NI (2015). Provenance and tectonic setting of Miocene siliclastic sediments, Sibuti Formation, northwestern Borneo. Arab J Geosci 8: 8549-8565.

Nagarajan R, Madhavaraju J, Nagendra R, Armstrong-Altrin JS, Moutte J (2011). Geochemistry of Neoproterozoic shales of the Rabanpalli Formation Bhima Basin, Northern Karnataka, southern India: implications for provenance and paleoredox conditions. Rev Mex Cien Geol 24: 20-30.

Nath BN, Bau M, Ramalingeswara Rao B, Rao CM (1997). Trace and rare earth elemental variation in Arabian Sea sediments through a transect across the oxygen minimum zone. Geochim Cosmochim Ac 61: 2375-2388.

Nemecz E (1981). Clay Minerals. Budapest, Hungary: Akadémiai Kiadó.

Nesbitt HW, Fedo CM, Young GM (1997). Quartz and feldspar stability, steady and non-steady state weathering and petrogenesis of siliciclastic sands and muds. J Geol 105: 173-191.

Nesbitt HW, Young GM (1982). Early Proterozoic climates and plate motions inferred from major element chemistry of lutites. Nature 299: 715-717.

Nesbitt HW, Young GM (1984). Prediction of some weathering trends of plutonic and volcanic rocks based upon thermodynamic and kinetic consideration. Geochim Cosmochim Ac 48: 1523-1534.

Nesbitt HW, Young GM (1996). Petrogenesis of sediments in the absence of chemical weathering: effects of abrasion and sorting on bulk composition and mineralogy. Sediment 43: 341-358.

Numan NMS (1997). A plate tectonic scenario for the Phanerozoic succession in Iraq. Iraqi Geol Jour 30: 1-28.

Oliveira A, Rocha F, Rodrigues A, Jouanneau JM, Dias A, Weber O, Gomes C (2002). Clay minerals from the sedimentary cover from Northwest Iberian Shelf. Prog Ocean 52: 233-247.

Rimmer SM (2004). Geochemical paleoredox indicators in Devonian-Mississippian black shales, Central Appalachian Basin (USA). Chem Geol 206: 373-391.

Roser BP, Korsch RJ (1986). Determination of tectonic setting of sandstone-mudstone suites using SiO_2 content and K_2O/Na_2O ratio. J Geol 94: 635-650.

Roser BP, Korsch RJ (1988). Provenance signatures of sandstone mudstone suites determined using discriminant function analysis of major-element data. Chem Geol 67: 119-139.

Ryan KM, Williams DM (2007). Testing the reliability of discrimination diagrams for determining the tectonic depositional environment of ancient sedimentary basins. Chem Geol 242: 103-25.

Sari A, Koca D (2012). An approach to provenance, tectonic and redox conditions of Jurassic-Cretaceous Akkuyu Formation, Central Taurids, Turkey. Mineral Res Explor Bull 144: 51-74.

Schreiber UM, Eriksson PG, Van der Neut M, Snyman CP (1992). Sedimentary petrography of the Early Proterozoic Pretoria Group, Transvaal Sequence, South Africa: implications for tectonic setting. Sediment Geol 80: 89-103.

Sharland PR, Archer R, Casey DM, Davies RB, Hall SH, Heward AP, Horbury AD, Simmons MD (2001). Arabian Plate Sequence Stratigraphy. GeoArabia, Special Publication 2. Manama, Bahrain: Gulf PetroLink.

Singh P (2009). Major, trace and REE geochemistry of the Ganga River sediments: influence of provenance and sedimentary processes. Chem Geol 266: 242-255.

Singh P (2010). Geochemistry and provenance of stream sediments of the Ganga River and its major tributaries in the Himalayan region, India. Chem Geol 269: 220-236.

Tao H, Sun S, Wang Q, Yang X, Jiang L (2014) Petrography and geochemistry of Lower Carboniferous greywacke and mudstones in northeast Junggar, China: implications for provenance, source weathering, and tectonic setting. J Asian Earth Sci 87:11-25.

Tawfik HA, Ghandour IM, Maejima W, Armstron-Altrin JS, Abdel-Hameed AT (2015). Petrography and geochemistry of the siliciclastic Araba Formation (Cambrian), east Sinai, Egypt: implications for provenance, tectonic setting and source weathering. Geol Mag (in press).

Taylor SR, McLennan SH (1985). The geochemical evolution of the continental crust. Rev Geophys 33: 241-265.

Valloni R, Maynard B (1981). Detrital modes of recent deep-sea sands and their relation to tectonic setting: a first approximation. Sediment 28: 75-83.

Verma SP, Armstrong-Altrin JS (2013). New multi-dimensional diagrams for tectonic discrimination of siliclastic sediments and their application to Precambrian basins. Chem Geol 355: 117-133.

Verma SP, Armstrong-Altrin JS (2016). Geochemical discrimination of siliclastic sediments from active and passive margin settings. Sediment Geol 332: 1-12.

Wrafter JP, Graham JR (1989). Ophiolitic detritus in the Ordovician sediments of 700 South Mayo, Ireland. J Geol Soc London 146: 213-215.

Yan Y, Xia B, Lin CX, Hu XQ, Yan P, Zhang F (2007). Geochemistry of the sedimentary rocks from the Nanxiong Basin, South China and implications for provenance, paleoenvironment and paleoclimate at the K/T boundary. Sediment Geol 197: 127-140.

Zaid SM (2015) Geochemistry of sandstones from the Pliocene Gabir Formation, north Marsa Alam, Red Sea, Egypt: implication for provenance, weathering and tectonic setting. J Afr Earth Sci 102: 1-17.